

University of Groningen

Differential scaling between G1 protein production and cell size dynamics promotes commitment to the cell division cycle in budding yeast

Litsios, Athanasios; Huberts, Daphne H E W; Terpstra, Hanna M; Guerra, Paolo; Schmidt, Alexander; Buczak, Katarzyna; Papagiannakis, Alexandros; Rovetta, Mattia; Hekelaar, Johan; Hubmann, Georg

Published in:
 Nature Cell Biology

DOI:
[10.1038/s41556-019-0413-3](https://doi.org/10.1038/s41556-019-0413-3)

IMPORTANT NOTE: You are advised to consult the publisher's version (publisher's PDF) if you wish to cite from it. Please check the document version below.

Document Version
Final author's version (accepted by publisher, after peer review)

Publication date:
2019

[Link to publication in University of Groningen/UMCG research database](#)

Citation for published version (APA):

Litsios, A., Huberts, D. H. E. W., Terpstra, H. M., Guerra, P., Schmidt, A., Buczak, K., Papagiannakis, A., Rovetta, M., Hekelaar, J., Hubmann, G., Exterkate, M., Miliadis-Argeitis, A., & Heinemann, M. (2019). Differential scaling between G1 protein production and cell size dynamics promotes commitment to the cell division cycle in budding yeast. *Nature Cell Biology*, 21(11), 1382-1392. <https://doi.org/10.1038/s41556-019-0413-3>

Copyright

Other than for strictly personal use, it is not permitted to download or to forward/distribute the text or part of it without the consent of the author(s) and/or copyright holder(s), unless the work is under an open content license (like Creative Commons).

Take-down policy

If you believe that this document breaches copyright please contact us providing details, and we will remove access to the work immediately and investigate your claim.

Downloaded from the University of Groningen/UMCG research database (Pure): <http://www.rug.nl/research/portal>. For technical reasons the number of authors shown on this cover page is limited to 10 maximum.

1
2
3
4
5
6
7
8
9
10
11
12
13
14
15
16
17
18
19
20
21
22
23
24
25
26
27
28
29
30
31
32
33
34
35
36
37
38
39
40
41
42
43

Differential scaling between G1 protein production and cell size dynamics promotes commitment to the cell division cycle in budding yeast

Athanasios Litsios¹, Daphne H. E. W. Huberts^{1,2}, Hanna Terpstra¹, Paolo Guerra¹, Alexander Schmidt³, Katarzyna Buczak³, Alexandros Papagiannakis¹, Mattia Rovetta¹, Johan Hekelaar¹, Georg Hubmann^{1,4}, Marten Exterkate^{1,5}, Andreas Miliadis-Argeitis^{1,6}, Matthias Heinemann^{1,6,*}

¹Molecular Systems Biology
Groningen Biomolecular Sciences and Biotechnology Institute, University of Groningen, Nijenborgh 4,
9747 AG Groningen, Netherlands

²Present address: Cancer Research UK Cambridge Institute
University of Cambridge, Li Ka Shing Centre, Robinson Way, Cambridge CB2 0RE, UK

³Proteomics Core Facility
Biozentrum, University of Basel, 4056 Basel, Switzerland

⁴Present address: Department of Biology, Laboratory of Molecular Cell Biology, Institute of Botany
and Microbiology, KU Leuven, & Center for Microbiology, VIB, Kasteelpark Arenberg, 31, 3001
Heverlee, Belgium

⁵Present address: Molecular Microbiology,
Groningen Biomolecular Sciences and Biotechnology Institute, University of Groningen, Nijenborgh 7,
9747 AG Groningen, Netherlands

⁶Corresponding authors

*Lead contact: m.heinemann@rug.nl

44 **ABSTRACT**

45 In the unicellular eukaryote *Saccharomyces cerevisiae*, Cln3-CDK activity enables Start, the irreversible
46 commitment to the cell division cycle. However, the concentration of Cln3 has been paradoxically
47 considered to remain constant during G1, due to the presumed scaling of its production rate with cell
48 size dynamics. Measuring metabolic and biosynthetic activity during cell cycle progression in single
49 cells, we found that cells exhibit pulses in protein production rate, which do not scale with cell size
50 dynamics, but, following the intrinsic metabolic dynamics, peak around Start. Using a viral-based
51 bicistronic construct and targeted proteomics to measure Cln3 at the single-cell and population levels,
52 we show that the differential scaling between protein production and cell size leads to a temporal
53 increase in Cln3 concentration, and passage through Start. This differential scaling causes Start in both
54 daughter and mother cells across growth conditions. Thus, uncoupling between two fundamental
55 physiological parameters drives cell cycle commitment.

56 **INTRODUCTION**

57 The cell division cycle is the process by which eukaryotic cells replicate themselves. Cells irreversibly
58 commit to enter the cell cycle after passing through a checkpoint located in late G1, known as Start in
59 budding yeast, or the restriction point in mammals¹. The most upstream activator of Start is Cln3²⁻⁴, a
60 highly unstable G1 cyclin⁵. In complex with the cyclin-dependent kinase Cdc28, Cln3 activates Start by
61 de-repressing SBF/MBF-related transcription via phosphorylation of the transcriptional inhibitor
62 Whi5^{6,7} and also via Whi5-independent means⁸. Cln3-mediated de-repression of transcription leads to
63 the activation of a positive feedback loop involving SBF and the late G1 cyclins Cln1/2, which locks the
64 transition from the G1 to the S phase of the cell cycle⁹.

65 Although it has long been known that Cln3 overexpression triggers early passage through Start, and
66 thus, Cln3 is a rate-limiting activator of Start²⁻⁴, the dynamics of Cln3 protein concentration during the
67 cell cycle are still largely enigmatic. While the mRNA of CLN3 appears to oscillate during the cell cycle,
68 with a peak around the M/G1 transition^{4,10}, the dynamics of the Cln3 protein are unclear. Early bulk
69 measurements with cells from synchronous cultures suggested that there are no cell-cycle related
70 fluctuations in Cln3 levels⁴. However, later population-level studies pointed towards changes in Cln3
71 abundance during G1^{11,12}. Determination of Cln3 levels via microscopy has so far remained impossible,
72 likely due to the instability of the protein⁵ and its low abundance. Time-lapse microscopy with
73 hyperstable Cln3 mutants, however, suggested that the concentration of Cln3 remains constant during
74 G1¹³. Thus, despite its key position in the Start network, the dynamics of this critical cell cycle regulator
75 remain elusive.

76 The abundance of Cln3 is considered to be directly dependent on the rate of protein production¹⁴, due
77 to the instability of Cln3 and the sensitivity of its translation rate to overall translation initiation¹⁵.
78 However, the dynamics of the protein production rate and cell size during G1 are also still rather
79 elusive, and thus, it is unclear how they together influence the concentration of Cln3. It is generally
80 assumed that protein production rate scales with cell size¹⁴, according to which the concentration of
81 Cln3 would remain constant during the cell cycle^{13,16}. However, it is unclear whether this parallel scaling
82 is correct: while the rate of protein production has been described to either increase exponentially
83 during the cell cycle^{17,18} or to remain constant¹⁹, the rate of cell size increase has been found to be
84 exponential^{20,21}, biphasic with two distinct linear growth phases¹⁹, or even to have more complex
85 dynamics^{22,23}. Thus, despite being fundamental physiological parameters, the dynamics of the protein
86 production rate and cell size during the cell cycle, and thus, their relationship and effect on Cln3
87 dynamics, remain unclear.

88 Despite the ambiguity in Cln3 dynamics, all prevalent models for Start assume a constant Cln3
89 concentration during G1^{8,13,24,25}. For instance, it was suggested that with constant Cln3 concentration,
90 the increase in the absolute number of Cln3 molecules during G1 would promote Start by saturating a
91 fixed number of SBF binding sites⁸. However, more recent work suggested that the ratio between Cln3
92 and Whi5 levels is what determines Start independently of DNA content¹³. Alternatively, it was
93 proposed that release of ER-retained Cln3 during G1 leads to an increase in nuclear Cln3 concentration
94 and promotion of Start^{24,25}. However, a recent localization analysis with a hyperstable Cln3 mutant did
95 not show any change in the enrichment of Cln3 in the nucleus during G1¹³. Finally, also assuming a
96 constant Cln3 concentration, it was proposed that Start is triggered by the dilution of the Start-inhibitor
97 Whi5¹³. However, a recent study did not detect any decrease in Whi5 concentration during G1²⁶.
98 Moreover, while the Whi5-dilution model assumes that the increase of cell size during G1 determines
99 the timing of Start, a lack of correlation between the rate of cell proliferation and cell size was recently
100 reported²⁷, leaving unclear how the respective model applies across growth conditions.

101 A so far underrated element of Start control is the intrinsic dynamics of metabolism during the cell
102 cycle^{28,29}. Metabolic oscillations in the hour-scale, although autonomous from the cell cycle^{29,30}, are
103 strongly coupled to cell cycle progression across growth conditions^{29,31}, with the period around Start
104 being characterized by an increase in flux through central carbon metabolism³². Metabolism is linked
105 to Start, at least partially, via acetyl-CoA, a metabolite of glucose catabolism, which induces the
106 transcription of CLN3 along with ribosomal and other growth genes through promotion of histone
107 acetylation³³. Also, it was suggested that metabolic inputs may shape cell cycle decisions by influencing
108 the rate of protein production³⁴. Nevertheless, it was only until recently that indication was obtained

109 that metabolic oscillations dynamically gate Start²⁹, but how metabolic oscillations influence the
110 commitment to the division cycle remains largely unknown.

111 Here, using microfluidics and time-lapse microscopy to measure simultaneously cell cycle,
112 biosynthetic, and metabolic activity in individual *Saccharomyces cerevisiae* cells, we found that at
113 constant nutrient conditions cells display a pulse in protein production rate during G1, which (i)
114 requires a sufficient flux through central carbon metabolism, (ii) does not scale with cell size dynamics,
115 and (iii) is essential for passage through Start. Using a viral-based bicistronic construct to overcome
116 the chronic technical hurdle of determining the concentration of wild type Cln3 *in vivo*, and targeted
117 proteomics, we show that this differential scaling between protein production rate and cell size
118 dynamics leads to a severalfold increase in Cln3 concentration in G1, causing Start. Moreover, we
119 demonstrate that this differential scaling explains Start across different growth conditions and in both
120 daughter and mother cells. Our results resolve a nearly two-decade long enigma, showing that the
121 uncoupling of two fundamental physiological parameters promotes the commitment to the cell
122 division cycle.

123 **RESULTS**

124 **Cells with low glycolytic flux generate biomass, but fail to pass Start**

125 Towards understanding the impact of metabolic oscillations on cell cycle control, we first asked if Start
126 depends on the level of flux through central carbon metabolism. To test this, we used microfluidics^{35,36}
127 and microscopy to monitor the budding activity of hundreds of individual cells of a strain (TM6*) that,
128 compared to wild type, displays a ≈5-fold reduced glycolytic flux in glucose-rich conditions, due to the
129 expression of only a chimeric hexose transporter (HXT) gene instead of the native HXTs³⁷. We found
130 that on high glucose (10 gL⁻¹), a fraction of cells (3.06% ± 0.96%; mean ± SEM, 4 independent biological
131 experiments, n=966 cells) remained unbudded during the ≥ 40-hour observation period (Figure 1a), in
132 contrast to wild type, where all cells budded (n=789 cells). To test if these non-dividing cells are viable,
133 we assessed their capacity to produce biomass. We found that the non-dividing cells increased in
134 volume nearly two-fold over time (Figure 1b), and also almost tripled their GFP content when GFP was
135 expressed via a constitutive promoter (Figure 1c; Extended Data Figure 1a), demonstrating their
136 viability. Using the localization of the transcriptional inhibitor Whi5 as a reporter of cell cycle phase,
137 we found that all non-dividing cells were arrested in G1, and thus, had not undergone Start (Extended
138 Data Figure 1b).

139 To test if the G1-arrested cells had lower glucose uptake rate compared to coexisting dividing cells, we
140 provided the cells with a ≈20-min pulse of the fluorescent glucose analogue 2-[N-(7-nitrobenz-2-oxa-

141 1,3-diazol-4-yl) amino]-2-deoxy-d-glucose (2-NBDG), which is not metabolized further in glycolysis
142 after its uptake and phosphorylation³⁸. We found that the G1-arrested cells displayed significantly
143 lower increase in 2-NBDG fluorescence in comparison to the dividing cells (Figures 1d and 1e),
144 indicating that they indeed have a lower glucose uptake rate. Consistently, we found that feeding wild
145 type cells in the microfluidics device with steady, very low concentrations of glucose, which at around
146 0.025 gL⁻¹ becomes limiting for glucose uptake³⁹, led to up to ~80% of G1-arrested cells in the
147 population (Extended Data Figure 1d). These findings indicate that cells with low glycolytic flux are able
148 to produce biomass and increase in size, but fail to pass Start.

149 **High glycolytic flux enables Start by allowing for fast protein production**

150 To test if the low metabolic flux was indeed limiting for Start, we constructed a strain in which glycolytic
151 flux could be orthogonally controlled in an otherwise unaltered nutrient environment. Specifically,
152 because in single-HXT strains the glucose uptake rate directly correlates with Hxt expression levels⁴⁰,
153 we introduced the glucose transporter gene HXT1 under the control of a tetracycline inducible
154 promoter in a strain lacking all native glucose transporters⁴¹. In the absence of tetracycline, we found
155 that leaky Hxt1 expression (Extended Data Figure 1e) led to the coexistence of dividing and non-
156 dividing cells (~8% of 220 cells, observed for over 16 h), similarly to what we observed in the other low-
157 flux strain (TM6*). Whi5-GFP localization demonstrated that also these non-dividing cells were
158 arrested in G1 (Extended Data Figure 1b). Upon induction of Hxt1 expression, 94.9% of the G1-arrested
159 cells passed Start (Figure 1f). Start occurred only after the increase in Hxt1 levels, as shown with an
160 Hxt1-GFP fusion (Figure 1f inset). Similarly, we found that the low-flux TM6* G1-arrested cells could
161 also pass Start in response to increased glycolytic flux, accomplished by switching the feed from
162 glucose to maltose (Extended Data Figures 1f and 1g). Note that maltose also fuels glycolysis, but in
163 the TM6* strain with a higher rate compared to glucose (Extended Data Figure 1f), since it is taken up
164 via HXT-independent transport⁴². These experiments show that the level of glycolytic flux can be rate-
165 limiting for Start.

166 We hypothesized that the increase in glycolytic flux enables Start by allowing for faster protein
167 production. To test this, we first determined the rate of protein production in the low-flux TM6* G1-
168 arrested cells and in the coexisting high-flux dividing cells. Specifically, we determined the rate of
169 yEGFP accumulation in newly born cells (Figure 1g – upper panel), when yEGFP was expressed from a
170 constitutive Tet-On promoter⁴³. We found that following cell birth, the low-flux G1-arrested cells had
171 significantly lower rates of protein production compared to cells that managed to pass Start (Figure 1g
172 – lower panel). When we shifted the cells from glucose to maltose, which leads to substantial increase
173 in glycolytic flux (Extended Data Figure 1f), we found that the G1-arrested cells displayed a pulse in the

174 rate of protein production before passage through Start (Extended Data Figure 1h). To obtain the time
175 evolution of single-cell GFP production rates, we first smoothed the total GFP abundance time series
176 of each cell by fitting a Gaussian process model, and then calculated the derivative of the Gaussian
177 process posterior function (see Methods). We observed the same pulse response when we shifted wild
178 type cells arrested in G1 on low (0.01 gL^{-1}) glucose, to high (20 gL^{-1}) glucose (Figure 1h). We found that
179 the increase in the rate of protein production upon increase of glycolytic flux was necessary for Start,
180 since addition of $100 \mu\text{gL}^{-1}$ cycloheximide (60 min after the switch to high glucose) prevented cells from
181 undergoing Start (Figures 1h and 1i). Thus, an induced increase in glycolytic flux leads to a pulse in the
182 rate of protein production, which is required for passage through Start.

183 **Cells in steady nutrient conditions exhibit pulses in protein production in synchrony with metabolic** 184 **oscillations**

185 Next, we asked whether the intrinsic dynamics of metabolism during the cell cycle^{28,29} are related to
186 changes in the overall rate of protein production. First, we confirmed that also in wild type cells
187 growing at steady-state conditions, there is an increase in glucose uptake rate during G1 (Figures 2a-
188 2c). Then, to test the connection between metabolic and protein production dynamics, we measured
189 in single cells the production rate of sfGFP (driven by the TEF1 promoter) while concomitantly
190 monitoring NAD(P)H autofluorescence^{29,44}, which has been previously used to report glycolytic flux
191 dynamics in yeast⁴⁵ (Extended Data Figures 2a and 2b). To define the timing of Start, we recorded the
192 localization of Whi5-mCherry. We found that during unperturbed growth, cells displayed pulses in
193 protein production rate during G1, which were in phase with the NAD(P)H oscillations, and coincided
194 with Start (Figures 2d, 2e, and Extended Data Figures 2c-2e).

195 To test if the dynamic changes of metabolism were necessary for the pulses in the protein production
196 rate, we perturbed glycolytic flux during G1 by temporarily adding to the 20 gL^{-1} glucose medium, 2 gL^{-1}
197 of the non-metabolizable glucose analogue 2-Deoxy-D-glucose (2-DG), which is taken up,
198 phosphorylated by hexokinase, but not metabolized further into glycolysis⁴⁶. We found that the
199 addition of 2-DG prevented the increase in NAD(P)H levels during G1 (Figure 2f), dramatically reduced
200 the rate of protein production (Figure 2g), and prevented cells from undergoing Start (Figure 2h). In
201 turn, removal of 2-DG led to increase in NAD(P)H levels, recovery of the protein production rate, and
202 subsequent passage through Start (Figures 2f-2h). Thus, under steady conditions, cells exhibit pulses
203 in the rate of protein production, which are in synchrony with metabolic oscillations and are essential
204 for Start.

205 **The pulses in the rate of protein production follow the metabolic, rather than the cell size dynamics**

206 Next, we checked whether the dynamics of the protein production rate follow the dynamics of cell size
207 during G1, as previously conjectured^{13,16}. Here, while the protein production rate scaled globally with
208 cell size (mean cell size during G1 versus mean production rate during G1; Spearman r : 0.596, p -value
209 <0.0001 , $n=50$ cells), we found that the dynamic changes in the rate of protein production were not
210 accompanied by respective changes in cell size during G1 in single cells. Specifically, while the rate of
211 protein production displayed a pulse-like behaviour, cell size increased continuously during G1 almost
212 until the bud emerged (Figure 3a, Extended Data Figures 3a and 3b). At the peak of the pulse, the
213 increase in the rate of protein production during G1 was on average nearly 1.5 to 2-fold higher than
214 the respective increase in cell size (Figure 3b, Extended Data Figure 3b). These findings indicate that
215 the dynamics of protein production rate are not coupled to those of cell size during the cell cycle.
216 Remarkably, we observed the uncoupling between protein production rate and cell size dynamics in
217 both small and large cells (Figures 3c-3e), as well as in cells that occasionally displayed more than one
218 pulse in protein production during a longer-than-usual G1, where protein production rate also
219 correlated with the intrinsic metabolic dynamics, but not with cell size dynamics (Figure 3f, Extended
220 Data Figures 3c and 3d). Collectively, these findings demonstrate that, contrary to common
221 assumptions, protein production and cell size dynamics scale differently during G1.

222 **Cln3 concentration increases severalfold around Start as a result of the pulse in protein production**

223 Given the differential scaling between protein production rate and cell size dynamics, we hypothesized
224 that the concentration of Cln3 could increase during G1, in case Cln3 production has a similar profile
225 as the TEF1-driven sfGFP production. In fact, TEF1 is a growth gene and transcription of CLN3 along
226 with growth and ribosomal genes has been shown to be metabolically-induced³³. However, unlike
227 sfGFP alone, Cln3-sfGFP cannot be detected, likely due to fast degradation of the protein fusion, which
228 does not leave sufficient time for fluorophore maturation after translation (Extended Data Figures 4a
229 and 4b). To overcome the technical limitation of measuring the *in vivo* production dynamics of the wild
230 type Cln3, we generated a genomic fusion of Cln3 and sfGFP at the endogenous CLN3 locus, with a
231 sequence encoding for a 2A self-cleaving peptide from the porcine teschovirus-1 added in-between
232 the two genes (Figure 4a). Since 2A peptides undergo non-enzymatic self-cleavage co-translationally,
233 proteins linked by 2A peptides are synthesized stoichiometrically, but exist after translation as two
234 unlinked proteins⁴⁷. Thus, using a genomic Cln3-2A-sfGFP fusion, we could uncouple the post-
235 translational fate of Cln3 and sfGFP, and despite the fast Cln3 degradation, sfGFP remained
236 undegraded and detectable (Figure 4b). In this way, by measuring the dynamic production rate of
237 sfGFP, we could estimate that of Cln3.

238 To confirm that Cln3-2A-sfGFP reports Cln3 production, we mutated the uORF at position –315 in the
239 5' mRNA leader of CLN3. Consistent with the function of the uORF to suppress Cln3 translation in slow
240 growth conditions¹⁵, we observed a ≈50% increase in sfGFP produced via the Cln3-2A-sfGFP fusion in
241 the A-315T/CLN3 strain compared to the wild type under such conditions (Extended Data Figure 4c).
242 Moreover, we found a good agreement between Cln3 levels determined via the Cln3-2A-sfGFP fusion
243 in single cells, and recently reported²⁷ bulk Cln3 measurements across different growth rates
244 (Extended Data Figure 4d). Thus, Cln3-2A-sfGFP expressed from the endogenous CLN3 promoter can
245 be used to determine Cln3 levels in single cells.

246 By determining the rate of sfGFP accumulation over time, we found that sfGFP from the Cln3-2A-sfGFP
247 fusion was also produced in pulses (Figure 4c, Extended Data Figures 4e-4i), similarly to sfGFP produced
248 by the TEF1 promoter (Figure 2d). We observed pulses with severalfold increase in the rate of Cln3
249 production (Figure 4c, Extended Data Figures 4h and 4i), again in contrast to the comparably small
250 increase in cell size (Extended Data Figures 4h and 4i). Taking into consideration that Cln3 abundance
251 is nearly proportional to Cln3 production rate (see Note in Methods and Extended Data Figure 8), and
252 employing the measured dynamic changes in cell size and sfGFP production rate, we calculated a
253 severalfold increase in the concentration of Cln3 during G1 (Figure 4d). To confirm that the
254 concentration of Cln3 increases during G1, we isolated small, unbudded G1 cells by centrifugal
255 elutriation, and performed targeted proteomics to measure Cln3 abundance during G1 progression. In
256 parallel, we determined cell size. Consistent with our single cell data, also here, we observed a pulse
257 in Cln3 abundance during G1 without an equivalent increase in cell size (Figure 4e), which together
258 resulted in an increase in Cln3 concentration (Figure 4f) before cell cycle commitment. Altogether,
259 these results demonstrate that the pulse in the rate of Cln3 production, and its mismatch with cell size
260 dynamics, lead to increase in the concentration of Cln3 in G1.

261 **The pulses in Cln3 concentration are responsible for Start**

262 To understand how this increase in Cln3 concentration contributes to Start, we measured also the
263 concentration dynamics of its target, Whi5. Here, we detected only a small or no change in Whi5
264 concentration during G1 by either microscopy or targeted proteomics measurements (Figure 5a,
265 Extended Data Figures 5a and 5b). In contrast, Cln3 concentration not only increased severalfold during
266 G1 (Figures 4d and 4f), but we found that the pulse in Cln3 production rate coincided with the time of
267 Start (Figure 5b). Furthermore, we determined the dynamics of Whi5 localization, along with the
268 dynamics of Cln3 and Cln2 production. We found that the increase in Cln3 production rate coincided
269 with the onset of Whi5 exit from the nucleus (Figure 5c), with the increase in Cln2 production following
270 closely afterwards, right before the complete translocation of Whi5 to the cytoplasm (Figure 5d). Thus,

271 the ordered occurrence of the pulse in Cln3 production, the onset of Whi5 translocation to the
272 cytoplasm, and the activation of Cln2 production, suggests that in the absence of major changes in
273 Whi5 concentration (Figure 5a, Extended Data Figure 5b), the increase in Cln3 concentration is the
274 primary cause for Start.

275 To confirm that the increase in Cln3 levels is the primary determinant of the timing of Start, we
276 decoupled the dynamics of Cln3 levels from the overall dynamics of protein production. To do this, we
277 allowed cells to undergo regular pulses in protein production rate, but dynamically prevented Cln3
278 levels from increasing, by enhancing the degradation rate of Cln3 via the auxin-inducible degron
279 (AID)^{51,52} (Figure 5e). In parallel, we monitored Whi5-mCherry localization dynamics to define Start,
280 and estimated the overall protein production dynamics by measuring sfGFP expressed via the TEF1
281 promoter. Here, we found that preventing Cln3 levels from increasing normally during the pulse in
282 protein production rate in wild type cells that were previously undergoing unperturbed cell division
283 cycles, and thus, cells that were adjusted to having normal Cln3 dynamics, led to an up to \approx 13-fold
284 increase in the median duration of pre-Start G1 (Figures 5f and 5g, Extended Data Figure 5c).
285 Interestingly, despite the remarkably long G1 duration, when Start occurred, it also here did so during
286 a pulse in protein production, which then had a nearly 2-fold higher peak rate compared to the normal
287 pulses (Figure 5f, Extended Data Figure 5d). These findings demonstrate that the dynamics of Cln3
288 constitute the primary determinant of the timing of Start.

289 **The differential scaling between Cln3 production rate and cell size dynamics explains Start across** 290 **different nutrient conditions and cell age**

291 As Start control has been so far almost exclusively studied in daughter cells, we then asked whether
292 the differential scaling between Cln3 production rate and cell size is responsible for Start also in
293 mothers. Indeed, we found that mother cells increased in cell size only marginally between cytokinesis
294 and Start, and Whi5 concentration remained constant during that time (Figure 6a). Furthermore,
295 similarly to daughters, mother cells displayed also a pulse in Cln3 production that coincided with Start
296 (Figure 6b), indicating that the same mechanism for Start applies also to mothers. Remarkably, the
297 pulse in Cln3 production was initiated already before cytokinesis and peaked shortly after the onset of
298 G1 phase (Figure 6b), possibly explaining the shorter G1 duration in mothers.

299 If the differential scaling between Cln3 production rate and cell size dynamics is the primary cause of
300 Start, we argued that apart from daughters and mothers on a certain nutrient, this mechanism has to
301 explain Start also across different growth conditions. While so far we focused on cells growing on
302 glucose, metabolic oscillations in synchrony with the cell cycle have been observed across nutrient
303 environments²⁹. Therefore, we measured the metabolic, biosynthetic, and cell cycle activity also under

304 different nutrient conditions, where doubling times ranged from ≈ 1.5 to more than 5.5 hours. Also
305 here, we observed small or no change in Whi5 concentration during G1 (Extended Data Figures 6a-6c),
306 but we found that cells exhibited pulses in the rate of protein production in synchrony with metabolic
307 oscillations (Extended Data Figures 6d and 6e), without corresponding increase in cell size (Extended
308 Data Figures 6f and 6g). Also under these growth conditions, Start occurred during the Cln3 pulse
309 (Figures 6c, 6d, Extended Data Figures 7a-7d). Thus, these data indicate that Cln3 concentration
310 dynamics determine the timing of Start across different nutrient conditions.

311 Finally, because during replicative ageing yeast cells undergo dramatic changes in their physiology,
312 even if nutrient conditions are retained constant⁵³, we asked whether the here identified mechanism
313 is responsible for Start also in replicatively aged cells. To test this, we used our microfluidic device to
314 obtain replicatively aged cells, and monitored Cln3 and Whi5 dynamics along with cell cycle
315 progression. Also in this case, we observed only minor changes in Whi5 concentration, and Start
316 occurred during pronounced pulses in Cln3 production (Figure 6e). These findings indicate that Cln3
317 dynamics are responsible for Start independently of cell age.

318 **DISCUSSION**

319 Using single-cell time-lapse fluorescence microscopy combined with meticulous image and data
320 analysis, we measured metabolic, biosynthetic, and cell cycle activity concomitantly, in unperturbed *S.*
321 *cerevisiae* cells growing at various steady and dynamic nutrient environments. We show that the
322 overall rate of protein production increases considerably more than cell size during G1, and thus, these
323 two fundamental physiological parameters do not scale with each other in the course of the cell cycle.
324 Using a viral-based bicistronic construct and targeted proteomics, we show that Cln3 is produced in
325 pulses, which follow the intrinsic metabolic dynamics, and which lead to increase in Cln3 production
326 rate that is proportionally larger than the respective increase of cell size during G1. This differential
327 scaling between Cln3 production rate and cell size dynamics leads to a severalfold increase in the
328 concentration of Cln3, causing cell cycle Start (Figure 6f). Collectively, we have identified a cause of
329 Start that is universal for daughter and mother cells, as well as across growth conditions.

330 Our finding that protein production rate displays a pulse-like behaviour contradicts early population-
331 and single-cell level measurements, which suggested an exponentially increasing rate of protein
332 production during the cell cycle^{17,18}. However, cell cycle dependent trends can be easily masked in
333 population-level experiments, and on the other hand, dynamic trends in single-cell approaches are
334 particularly prone to molecular and technical noise. In accordance with our results, recent single-cell
335 measurements showed a marked slowdown in the accumulation rate of a constitutively expressed
336 fluorescent protein during the G1-S transition¹⁹, indicative of the pulsing behaviour of protein

337 production rate that we describe here. Moreover, it was proposed that protein production decreases
338 as a result of induced polarization of the actin cytoskeleton²². Thus, our finding that the rate of protein
339 production decreases after Start following its pulse, is consistent with the fact that in late G1 there is
340 polarization of the actin cytoskeleton⁵⁴. Furthermore, the increase in cell density that has been
341 reported to occur around Start⁵⁵ could be explained by our finding that the disproportional increase of
342 protein production rate with respect to cell size is highest around this period.

343 The dynamics of Cln3 during G1 have remained elusive for almost two decades. Resolving the technical
344 hurdle of measuring the production rate of wild type Cln3 in single cells during the cell cycle utilizing a
345 viral-based bicistronic construct, and combining this with parallel cell size measurements, we found
346 that Cln3 concentration increases during G1. We confirmed the increase in Cln3 concentration during
347 G1 using targeted proteomics, thereby also confirming the assumption which underlies the
348 experiments with the bicistronic construct, i.e. that any potential temporal variations in the post-
349 translational regulation of Cln3 abundance (e.g. dynamics in Cln3 degradation) during G1 do not play
350 a major role. In contrast to previous attempts to quantify Cln3 levels in single cells¹³, we did not rely
351 on hyper-stabilized mutant versions of the Cln3 protein, whose dynamics are expected to be less
352 pronounced in comparison to those of wild type Cln3. Moreover, to account for inherent cell-to-cell
353 variability, we examined cell-cycle related Cln3 dynamics either in time-traces of individual cells, or in
354 averaged single-cell data aligned at the moment of Start, something which was not done earlier.

355 While it was recently proposed that the timing of Start is determined by the dilution of Whi5¹³,
356 accumulating evidence from more recent studies contradicts this model. In accordance with our
357 findings, Dorsey *et al.* did not observe any dilution of Whi5 in different genetic backgrounds and
358 nutrient conditions, attributing reported changes in Whi5 concentration to photobleaching²⁶.
359 Moreover, although the inhibitor dilution model suggests that the increase in cell size during G1
360 determines the timing of Start, it was recently shown that there is no significant correlation between
361 cell size and the rate of cell division²⁷, and thus, it is unclear how this model applies to different growth
362 conditions. Finally, even assuming cell size-dependent changes in Whi5 concentration during G1, the
363 Whi5-dilution model would fall short of robustly explaining the timing Start in mother yeast cells, given
364 that mother G1 is associated with very small changes in cell size (Figure 6a, Extended Data Figures 6b
365 and 6c), while G1 duration can remarkably vary (Figure 6d).

366 In contrast, as we show here, the differential scaling between protein production rate and cell size can
367 constitute a universal mechanism for Start, applying to both daughter and mother cells, as well as
368 across different growth conditions. We show that the increase in Cln3 concentration is the primary
369 trigger for the G1/S transition. Still, other mechanisms might act in parallel to fine-tune the timing of

370 Start. For example, as cells proceed through G1, the accumulation of the SBF-component Swi4²⁶
371 downstream of Cln3, or the chaperone-mediated release of ER-retained Cln3^{24,56} can potentially
372 further increase the probability of Start. It is possible that under specific growth conditions, changes
373 in Whi5 levels¹³ may also contribute to Start.

374 Furthermore, our findings show that the dynamics of protein production rate follow the intrinsic
375 metabolic dynamics, suggesting a connection between the two. Also, we show that high metabolic flux
376 enables the attainment of high overall protein, and by extension, Cln3 production rates. In fact, it was
377 hypothesized almost a decade ago that a metabolic burst during G1 could boost translation, and
378 thereby Cln3 production⁵⁷, although experimental evidence was missing. Nevertheless, the truth is
379 possibly more complex than simply metabolic dynamics governing protein production rates. In yeast
380 and higher eukaryotes, there are feedback interactions between metabolism and protein
381 production^{58,59}, and how exactly these processes influence each other in the course of the cell cycle
382 remains to be revealed.

383 Early work had suggested that Start relies on the attainment of a critical protein production rate⁶⁰
384 which is necessary for the accumulation of specific activating proteins, and it was conjectured already
385 by Unger and Hartwell that the unifying signal linking physiological status to the cell cycle decisions is
386 the rate of protein production³⁴. Our results demonstrate that this view was correct. Crucially,
387 however, we additionally show that increased protein production rates control cell cycle Start due to
388 the differential scaling between protein production rate and cell size during G1. Moreover, a
389 sufficiently strong metabolic flux is required for the attainment of high protein production rates,
390 suggesting that cells assess both their metabolic state and biosynthetic capacity before committing to
391 entering the cell division cycle.

392 Due to the high degree of conservation of core metabolism⁶¹ and the G1-control network across
393 eukaryotes⁶², we envision that similar principles for cell cycle commitment may apply also to higher
394 eukaryotes.

395 **ACKNOWLEDGEMENTS**

396 The authors thank Benjamin Tu for critical comments on an early version of the manuscript; Zheng
397 Zhang for advice on microscopy; Christoffer Åberg for discussions on model-based analysis of
398 microscopy data, and the Ida van der Klei lab for the kind provision of the pSNA10 plasmid. Financial
399 support was provided by the EU ITN project ISOLATE (grant agreement 289995).

400 **AUTHOR CONTRIBUTIONS**

401 A.L. and M.H. conceived the study. A.L., M.H. and A.M.-A. designed the study. A.L. constructed the
402 strains, performed the experiments, and analysed the data. D.H.E.W.H. performed preliminary
403 experiments and contributed conceptually. H.T. participated in strain construction and culture
404 sampling for targeted proteomics. A.M.-A. performed the smoothing and derivative estimation for the
405 single-cell time-lapse data. P.G. performed and analysed the verification experiments with confocal
406 microscopy. A.S. and K.B. performed targeted proteomics and analysed the data. A.P. participated in
407 strain construction, metabolite measurements during batch cultivation, and did preliminary data
408 analysis. M.R. performed the elutriation and participated in culture sampling for targeted proteomics
409 and respective data analysis. J.H. prepared protein samples for mass spectrometry. G.H. performed
410 the model-based analysis of the metabolite data for estimation of cellular physiology. M.E. participated
411 in strain construction. A.L. and M.H. wrote the manuscript with input from A.M.-A.. M.H. and A.M.-A.
412 supervised the study.

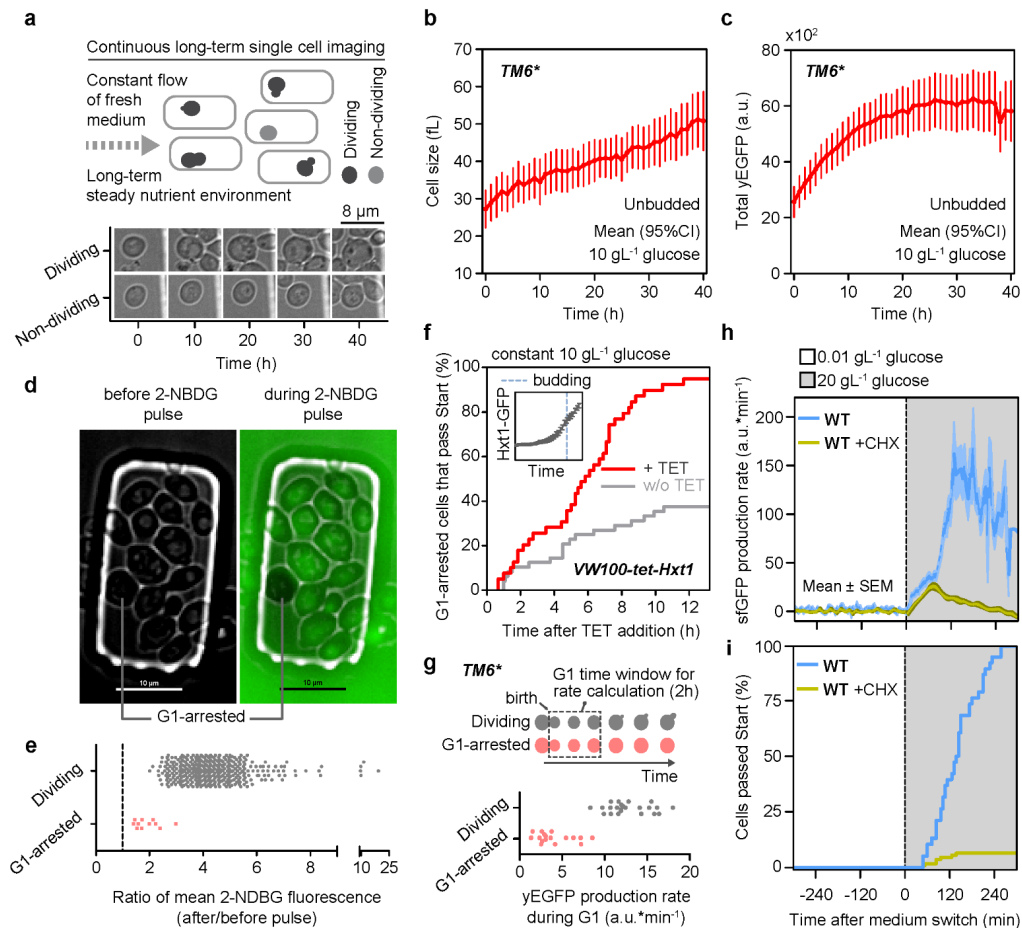
413 **DECLARATION OF INTERESTS**

414 The authors declare no competing interests.

415

416 .

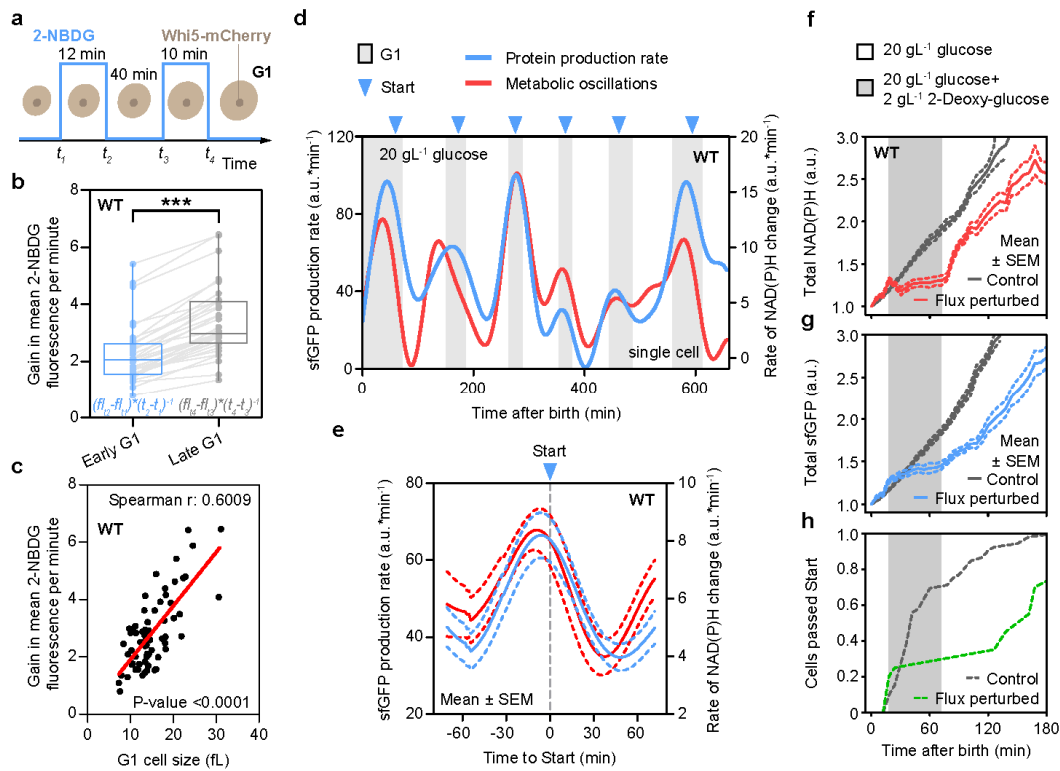
417



419

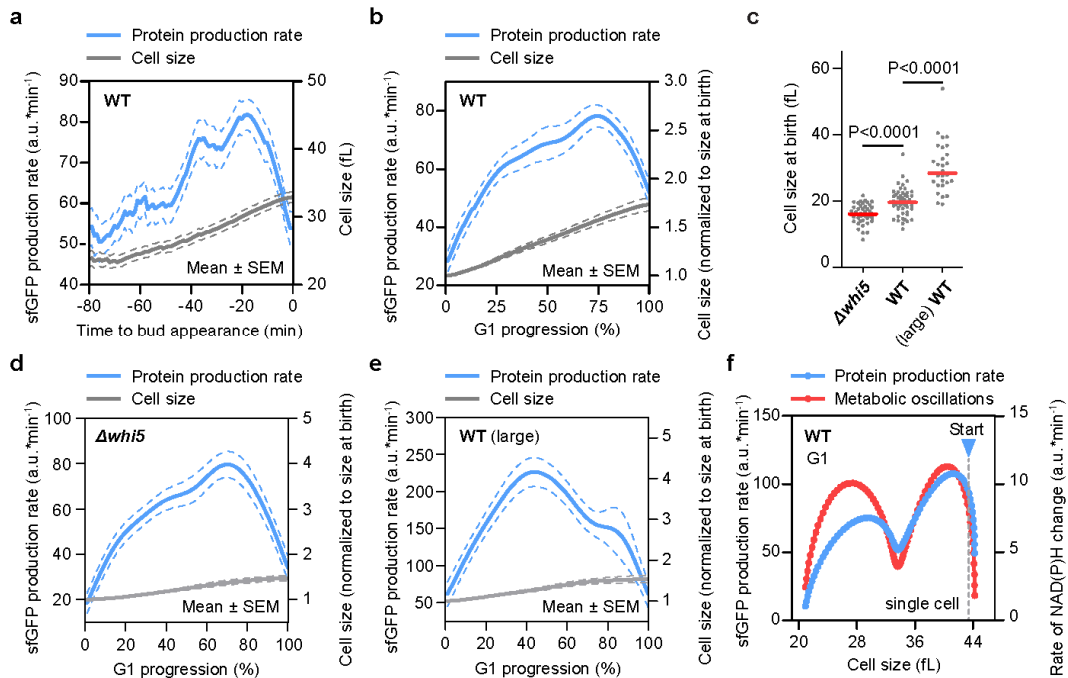
420 **Figure 1 | High glycolytic flux enables Start by allowing for fast protein production.** (a) Above: Schematic of
 421 microfluidics-based experimental setup. Cells are trapped underneath PDMS pads and continuously fed with
 422 fresh medium. Below: Time-lapse images of coexisting dividing and non-dividing cells. Experiment repeated
 423 independently 4 times with similar results. (b) Cell size ($n=18$ cells) and (c) total yEGFP content ($n=14$ cells) of
 424 non-dividing cells over time. yEGFP expressed via Tet-ON promoter⁴³ ($300 \text{ ng} \cdot \text{mL}^{-1}$ TET). (d) Merged phase-
 425 contrast and fluorescent images of $TM6^*$ cells (10 gL^{-1} glucose) before and during pulse with 0.01 gL^{-1} glucose
 426 supplemented with $60 \mu\text{M}$ 2-NBDG. Experiment performed once with multiple imaging positions. (e) Ratio of
 427 mean cellular 2-NBDG fluorescence after and before the pulse in G1-arrested (cells that remained unbudded for
 428 the whole observation period (>24 hours); $n=11$) and dividing cells (rest of the cells; $n=373$) (Mann Whitney test
 429 p -value <0.0001). Among dividing cells, a significant negative correlation between G1 duration and G1 glucose
 430 uptake rate was observed (Extended Data Figure 1c). (f) Percentage of G1-arrested cells ($n=39$ cells) that pass
 431 Start (as indicated by bud emergence) in response to addition of $50 \text{ ng} \cdot \text{mL}^{-1}$ TET. Control ($n=48$ cells): no TET
 432 (log-rank (Mantel-Cox) test p -value <0.001). Inset: Hxt1-GFP levels in response to TET addition in cells ($n=25$ cells)
 433 aligned for the moment of bud emergence. (g) Average protein (yeGFP) production rate during G1 in dividing

434 (n=23 cells) and G1-arrested (n=17 cells) TM6* cells. Gain in total yeGFP during the first 2 hours after birth was
 435 determined, and this value was divided by 120 to obtain per-minute yeGFP production rate. **(h)** Dynamics of
 436 protein (sfGFP) production rate in G1-arrested wild type cells (n=36 cells) and **(i)** respective fraction of cells that
 437 pass Start in response to increase in glycolytic flux achieved by switching the feed from 0.01 to 20 gL⁻¹ glucose.
 438 Control: 60 min after the switch to 20 gL⁻¹ glucose, 100 ng*mL⁻¹ CHX added (n=29 and 107 cells for **(h)** and **(i)**
 439 respectively). For **(i)**, log-rank (Mantel-Cox) test p-value <0.001. sfGFP expressed via the TEF1 promoter. Source
 440 data for **b-c** and **e-i** are provided in Source Data Figure 1.



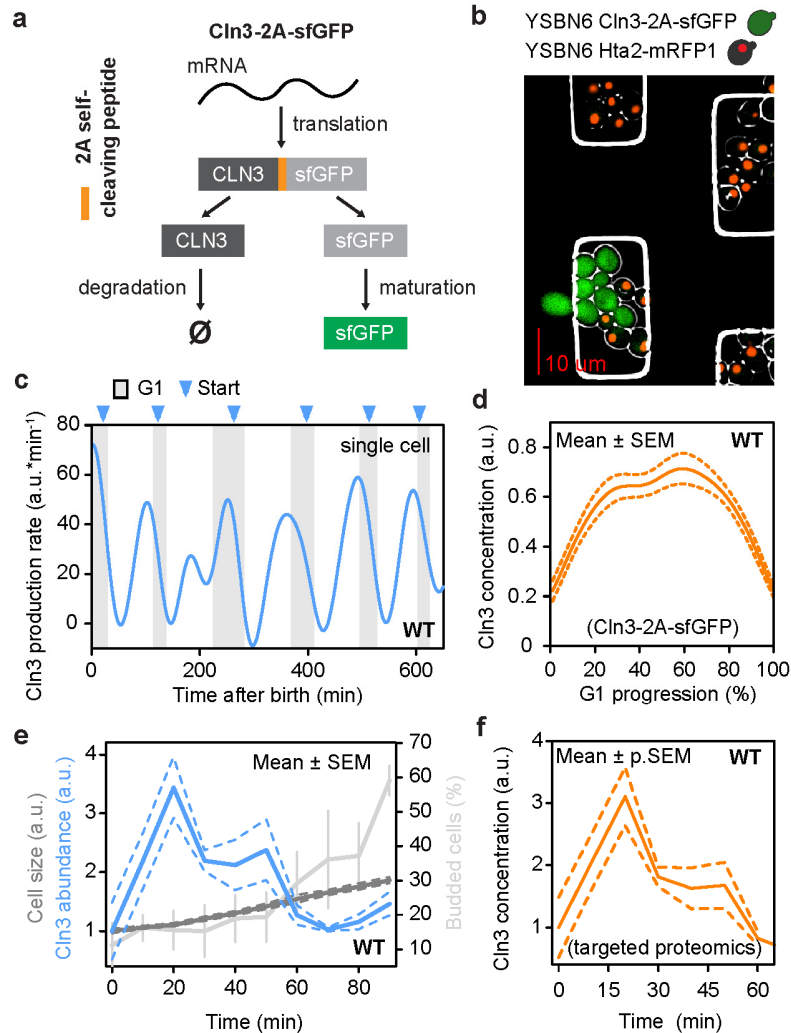
441
 442 **Figure 2 | At steady conditions, cells display pulses in the rate of protein production which are in synchrony**
 443 **with metabolic oscillations and are required for Start.** **(a)** Schematic representation of experiment for assessing
 444 glucose uptake rate dynamics during G1. G1 cells growing in 0.05 gL⁻¹ glucose were subjected to two subsequent
 445 pulses of 0.05 gL⁻¹ glucose plus 60 μM 2-NBDG. Whi5-mCherry localization was monitored in parallel, to detect
 446 cells that were in G1 and had not passed Start during either of the two pulses. In this way, the difference in
 447 glucose uptake rate between an early and a later G1 stage could be determined for the same single cell. **(b)**
 448 2-NBDG uptake in the same individual cells (n=33 cells) during the first and the second pulse (***) Wilcoxon signed
 449 rank test, p-value <0.0001. 2-NBDG uptake was estimated by calculating the gain in fluorescence per pulse ($f_{t_{n+1}}$
 450 $- f_{t_n}$) for each cell, and dividing it by the duration of each pulse ($t_{n+1} - t_n$). Boxplot: box extends from the 25th to
 451 75th percentiles and whiskers down to the min and up to the max value. **(c)** 2-NBDG uptake rate as a function of
 452 G1 cell size (n=66 cells). **(d)** Dynamics of sfGFP production rate and rate of NAD(P)H change in a single wild type
 453 cell at steady glucose (20 gL⁻¹) environment. **(e)** Dynamics of sfGFP production rate and rate of NAD(P)H change

454 in cells aligned for Start (n=16 cell cycles). Dynamics of (f) total NAD(P)H and total (g) sfGFP in response to
 455 addition and removal of 2-DG (2 gL⁻¹) in wild type cells (n=20 cells) growing in steady glucose (20 gL⁻¹)
 456 environment. Note that due to the abrupt effect of 2-DG on NAD(P)H and sfGFP dynamics, smoothing splines
 457 required for estimation of rates cannot reliably capture the timing of the changes, and thus, the respective
 458 NAD(P)H and sfGFP abundances are presented directly. (h) Cumulative distribution of cells (from f-g) passing
 459 Start. In the control experiments (grey lines; n=52 cells), no 2-DG was added. Source data for b-h are provided in
 460 Source Data Figure 2.



461

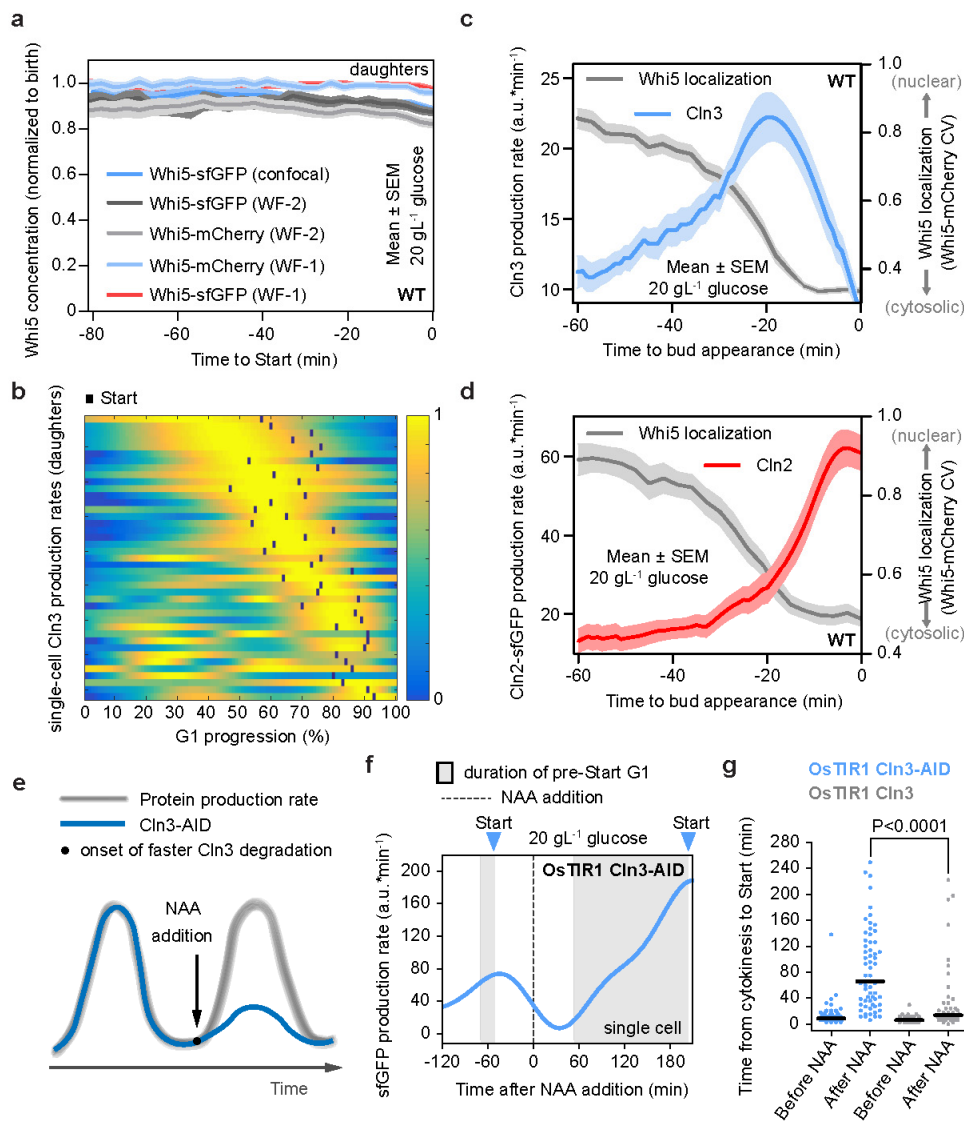
462 **Figure 3 | Cells display pulses in the rate of protein production during G1 which and are not accompanied by**
 463 **respective changes in cell size. (a)** sfGFP production rate and respective cell size dynamics in wild type daughter
 464 cells aligned for the moment of bud appearance (n=50 cells). (b) sfGFP production rate and respective cell size
 465 dynamics for normalized G1 progression in the same cells as in (a). (c) Cell size at birth in cells of the *Δwhi5* cell
 466 size mutant (n=44 cells), in wild type cells born by young mothers (WT, n=50 cells), and in wild type cells born by
 467 replicatively aged mothers ((large) WT, n=29 cells). Indicated p-values from Mann Whitney tests. Vertical lines
 468 denote the median. (d) sfGFP production rate and respective cell size dynamics for normalized G1 duration in
 469 *Δwhi5* mutants (n=44 cells) and (e) large wild type cells born by replicatively aged mothers (n=29 cells). (f)
 470 Dynamics of sfGFP production rate and rate of NAD(P)H change during G1 in a single wild type cell as a function
 471 of cell size. In all cases, sfGFP expression was driven by the TEF1 promoter. Source data for Figure 3 are provided
 472 in Source Data Figure 3.



473

474 **Figure 4 | Cln3 concentration changes severalfold during the cell cycle as a result of the pulse in its production**
 475 **rate, and the differential scaling between the latter and cell size dynamics.** (a) Incorporation of a viral self-
 476 self-cleaving peptide between Cln3 and sfGFP decouples the post-translational fate of Cln3 and sfGFP, allowing sfGFP
 477 to mature and report on Cln3 production rate. (b) Merged phase contrast and fluorescent (GFP and RFP channels)
 478 images of Cln3-2A-sfGFP wildtype cells mixed with wild type Hta2-mRFP1 cells as a control for cell
 479 autofluorescence at the GFP channel. Experiment was performed 3 times with similar results. (c) Dynamics of
 480 sfGFP production rate from the Cln3-2A-sfGFP fusion construct in a single cell. (d) Cln3 concentration dynamics
 481 in wild type daughter cells (n=41 cells) during normalized G1 progression. Since Cln3 is mainly nuclear^{13,48} and
 482 because the volume of the nucleus scales proportionally to cell volume^{49,50}, changes in the nuclear volume reflect
 483 changes in the measured cellular volume. Therefore, the concentration of Cln3 can be approximated by dividing
 484 its abundance (extracted from its production rate (see Methods)) with the cell volume. In (a-d), cells grew in a
 485 steady glucose (20 gL⁻¹) environment and Cln3 in fusion with the 2A-sfGFP construct was expressed from its
 486 endogenous locus. (e) Dynamics of Cln3 abundance identified by targeted proteomics, cell size, and budding
 487 index, in small, mostly unbudded G1 cells, which were isolated by centrifugal elutriation and released (t = 0) into

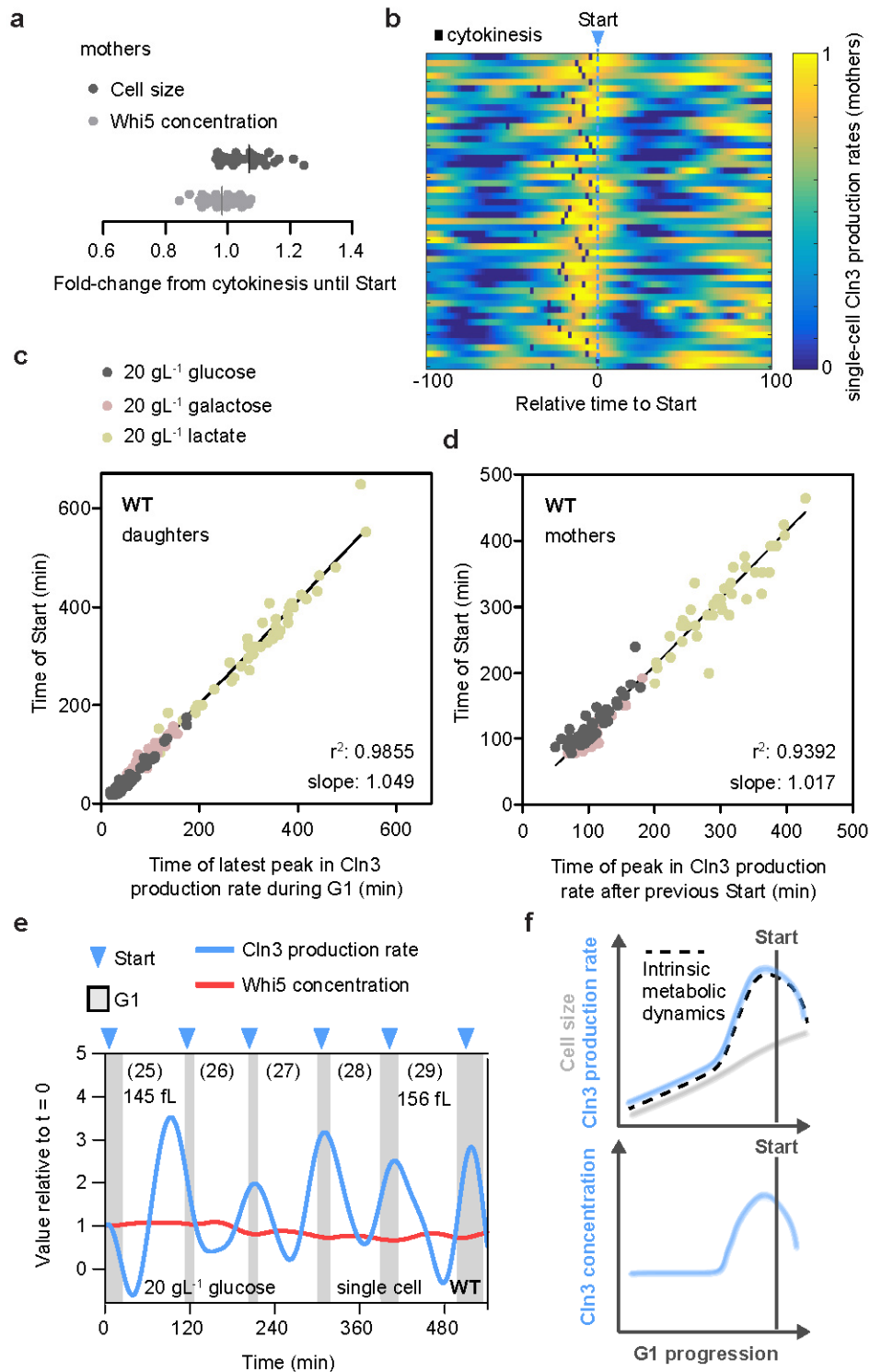
488 YPD (n=4 independent biological experiments). (f) Cln3 concentration during the early cell cycle estimated on the
 489 basis of the Cln3 abundance and cell size dynamics in (e). Error bars show propagated SEM. Cln3 and cell size
 490 data in (e) and (f) are normalized to t = 0. Source data for c-f are provided in Source Data Figure 4.



491

492 **Figure 5 | The Cln3 pulses determine the timing of Start.** (a) Whi5 concentration in daughter cells, normalized
 493 for concentration at birth and aligned for the moment of Start. For widefield experiments, n=101 and 50 cells for
 494 Whi5-sfGFP, and 52 and 50 cells for Whi5-mCherry, for WF-1 and WF-2, respectively (WF-1: mean cell
 495 fluorescence; WF-2: integrated fluorescence over whole cell area divided by cell volume). For confocal, n=44
 496 cells. (b) Heatmap showing the dynamics of the Cln3 production rate during G1 in single wild type daughter cells.
 497 For each cell, the Cln3 production rate time series was divided by the maximum value obtained during the
 498 corresponding observation window. The dark squares indicate the moment of Start in each cell. (c) Dynamics of
 499 Cln3 (n=41 cells) and (d) Cln2 (n=25 cells) production rate as a function of time and Whi5 localization in cells
 500 aligned for the moment of bud appearance. The production rate of Cln2 was estimated through a Cln2-sfGFP

501 fusion. **(e)** Schematic representation of induced Cln3 depletion in cells undergoing otherwise unperturbed cell
502 division cycles. The synthetic auxin substitute naphthalene-acetic acid (NAA) is added to cells which express the
503 plant F-box protein TIR1 and in which Cln3 is tagged with the auxin-inducible degron (AID). **(f)** Dynamics of sfGFP
504 production rate in a single OsTIR1 Cln3-AID cell treated with NAA at the indicated time point. Pre-Start G1 is
505 defined as the time of entry to G1 (cytokinesis) until the moment of Start. **(g)** Duration of pre-Start G1 before
506 (n=56 and 44 cells) and after (n=61 and 46 cells) addition of 1mM NAA in OsTIR1 Cln3-AID and OsTIR1 Cln3
507 (control) cells. Indicated p-value from Mann Whitney test. Horizontal lines denote the median. In **(f)** and **(g)**,
508 sfGFP is expressed via the TEF1 promoter. In all cases, cells grew in a steady glucose (20 gL^{-1}) environment, and
509 Start was determined via observation of Whi5-mCherry or Whi5-sfGFP localization. Source data for **a-d** and **f-g**
510 are provided in Source Data Figure 5.



511

512 **Figure 6 | The differential scaling between Cln3 production pulses and cell size dynamics constitutes a**
 513 **daughter/mother-, and growth-condition-independent cause of Start.** (a) Change in cell size and Whi5-sfGFP
 514 concentration (integrated fluorescence over whole cell area divided by cell volume) between cytokinesis and
 515 Start in mother cells (n=40 cells). The vertical lines denote the respective population average. (b) Heatmap

516 showing the dynamics of the Cln3 production rate in single wild type mother cells. Cells are aligned for Start ($t =$
517 0) and cytokinesis is indicated in each cell by a dark square. Data were normalized as in Figure 5b. (c) Time of
518 latest peak in Cln3 production rate during G1 versus the moment of Start in individual daughter cells ($n=120$ cells,
519 Spearman $r: 0.9875$), and (d) time of peak in Cln3 production rate after previous Start versus time between
520 previous and next Start in individual mother cells ($n=121$ cells, Spearman $r: 0.9415$) growing on different carbon
521 sources. (e) Cln3 production rate and Whi5 concentration dynamics in a single, wild-type, aged, large mother
522 cell. Numbers in parentheses indicate the replicative age of the mother at each Start event. The cell size of the
523 mother during the first and last displayed Start event is also shown. (f) Schematic representation of model for
524 cell cycle commitment. The differential scaling between the rate of Cln3 production and cell size dynamics during
525 G1 causes Start by leading to increase in Cln3 concentration. Source data for a-e are provided in Source Data
526 Figure 6.

527 REFERENCES

- 528 1. Johnson, A. & Skotheim, J. M. Start and the restriction point. *Curr. Opin. Cell Biol.* **25**, 717–23
529 (2013).
- 530 2. Nash, R., Tokiwa, G., Anand, S., Erickson, K. & Futcher, A. B. The WHI1+ gene of
531 *Saccharomyces cerevisiae* tethers cell division to cell size and is a cyclin homolog. *EMBO J.* **7**,
532 4335–46 (1988).
- 533 3. Cross, F. R. DAF1, a mutant gene affecting size control, pheromone arrest, and cell cycle
534 kinetics of *Saccharomyces cerevisiae*. *Mol. Cell. Biol.* **8**, 4675–84 (1988).
- 535 4. Tyers, M., Tokiwa, G. & Futcher, B. Comparison of the *Saccharomyces cerevisiae* G1 cyclins:
536 Cln3 may be an upstream activator of Cln1, Cln2 and other cyclins. *EMBO J.* **12**, 1955–68
537 (1993).
- 538 5. Tyers, M., Tokiwa, G., Nash, R. & Futcher, B. The Cln3-Cdc28 kinase complex of *S. cerevisiae* is
539 regulated by proteolysis and phosphorylation. *EMBO J.* **11**, 1773–84 (1992).
- 540 6. de Bruin, R. A. M., McDonald, W. H., Kalashnikova, T. I., Yates, J. & Wittenberg, C. Cln3
541 activates G1-specific transcription via phosphorylation of the SBF bound repressor Whi5. *Cell*
542 **117**, 887–98 (2004).
- 543 7. Costanzo, M. *et al.* CDK activity antagonizes Whi5, an inhibitor of G1/S transcription in yeast.
544 *Cell* **117**, 899–913 (2004).
- 545 8. Wang, H., Carey, L. B., Cai, Y., Wijnen, H. & Futcher, B. Recruitment of Cln3 cyclin to
546 promoters controls cell cycle entry via histone deacetylase and other targets. *PLoS Biol.* **7**,
547 e1000189 (2009).
- 548 9. Skotheim, J. M., Di Talia, S., Siggia, E. D. & Cross, F. R. Positive feedback of G1 cyclins ensures
549 coherent cell cycle entry. *Nature* **454**, 291–6 (2008).
- 550 10. McInerny, C. J., Partridge, J. F., Mikesell, G. E., Creemer, D. P. & Breeden, L. L. A novel Mcm1-
551 dependent element in the SWI4, CLN3, CDC6, and CDC47 promoters activates M/G1-specific
552 transcription. *Genes Dev.* **11**, 1277–1288 (1997).
- 553 11. Zapata, J. *et al.* PP2ARts1 is a master regulator of pathways that control cell size. *J. Cell Biol.*
554 **204**, 359–76 (2014).

- 555 12. Thorburn, R. R. *et al.* Aneuploid yeast strains exhibit defects in cell growth and passage
556 through START. *Mol. Biol. Cell* **24**, 1274–1289 (2013).
- 557 13. Schmoller, K. M., Turner, J. J., Kõivomägi, M. & Skotheim, J. M. Dilution of the cell cycle
558 inhibitor Whi5 controls budding-yeast cell size. *Nature* **526**, 268–72 (2015).
- 559 14. Jorgensen, P. & Tyers, M. How cells coordinate growth and division. *Curr. Biol.* **14**, R1014-27
560 (2004).
- 561 15. Polymenis, M. & Schmidt, E. V. Coupling of cell division to cell growth by translational control
562 of the G1 cyclin CLN3 in yeast. *Genes Dev.* **11**, 2522–31 (1997).
- 563 16. Schmoller, K. M. & Skotheim, J. M. The Biosynthetic Basis of Cell Size Control. *Trends Cell Biol.*
564 **25**, 793–802 (2015).
- 565 17. Elliott, S. G. & McLaughlin, C. S. Rate of macromolecular synthesis through the cell cycle of the
566 yeast *Saccharomyces cerevisiae*. *Proc. Natl. Acad. Sci. U. S. A.* **75**, 4384–8 (1978).
- 567 18. Di Talia, S., Skotheim, J. M., Bean, J. M., Siggia, E. D. & Cross, F. R. The effects of molecular
568 noise and size control on variability in the budding yeast cell cycle. *Nature* **448**, 947–51
569 (2007).
- 570 19. Cookson, N. A., Cookson, S. W., Tsimring, L. S. & Hasty, J. Cell cycle-dependent variations in
571 protein concentration. *Nucleic Acids Res.* **38**, 2676–81 (2010).
- 572 20. Soifer, I., Robert, L. & Amir, A. Single-Cell Analysis of Growth in Budding Yeast and Bacteria
573 Reveals a Common Size Regulation Strategy. *Curr. Biol.* **26**, 356–61 (2016).
- 574 21. Bryan, A. K., Engler, A., Gulati, A. & Manalis, S. R. Continuous and long-term volume
575 measurements with a commercial Coulter counter. *PLoS One* **7**, e29866 (2012).
- 576 22. Goranov, A. I. *et al.* The rate of cell growth is governed by cell cycle stage. *Genes Dev.* **23**,
577 1408–22 (2009).
- 578 23. Ferrezuelo, F. *et al.* The critical size is set at a single-cell level by growth rate to attain
579 homeostasis and adaptation. *Nat. Commun.* **3**, 1012 (2012).
- 580 24. Vergés, E., Colomina, N., Garí, E., Gallego, C. & Aldea, M. Cyclin Cln3 is retained at the ER and
581 released by the J chaperone Ydj1 in late G1 to trigger cell cycle entry. *Mol. Cell* **26**, 649–62
582 (2007).
- 583 25. Yahya, G., Parisi, E., Flores, A., Gallego, C. & Aldea, M. A Whi7-anchored loop controls the G1
584 Cdk-cyclin complex at start. *Mol. Cell* **53**, 115–26 (2014).
- 585 26. Dorsey, S. *et al.* G1/S Transcription Factor Copy Number Is a Growth-Dependent Determinant
586 of Cell Cycle Commitment in Yeast. *Cell Syst.* **6**, 539-554.e11 (2018).
- 587 27. Blank, H. M., Callahan, M., Pistikopoulos, I. P. E., Polymenis, A. O. & Polymenis, M. Scaling of
588 G1 Duration with Population Doubling Time by a Cyclin in *Saccharomyces cerevisiae*. *Genetics*
589 **210**, 895–906 (2018).
- 590 28. Tu, B. P., Kudlicki, A., Rowicka, M. & McKnight, S. L. Logic of the yeast metabolic cycle:
591 temporal compartmentalization of cellular processes. *Science* **310**, 1152–8 (2005).
- 592 29. Papagiannakis, A., Niebel, B., Wit, E. C. & Heinemann, M. Autonomous Metabolic Oscillations
593 Robustly Gate the Early and Late Cell Cycle. *Mol. Cell* **65**, 285–295 (2017).

- 594 30. Slavov, N., Macinskas, J., Caudy, A. & Botstein, D. Metabolic cycling without cell division
595 cycling in respiring yeast. *Proc. Natl. Acad. Sci. U. S. A.* **108**, 19090–5 (2011).
- 596 31. Burnett, A. J., Aydin, M. & Buchler, N. E. Cell cycle Start is coupled to entry into the yeast
597 metabolic cycle across diverse strains and growth rates. *Mol. Biol. Cell* **27**, 64–74 (2016).
- 598 32. Cai, L. & Tu, B. P. Driving the cell cycle through metabolism. *Annu. Rev. Cell Dev. Biol.* **28**, 59–
599 87 (2012).
- 600 33. Shi, L. & Tu, B. P. Acetyl-CoA induces transcription of the key G1 cyclin CLN3 to promote entry
601 into the cell division cycle in *Saccharomyces cerevisiae*. *Proc. Natl. Acad. Sci. U. S. A.* **110**,
602 7318–23 (2013).
- 603 34. Unger, M. W. & Hartwell, L. H. Control of cell division in *Saccharomyces cerevisiae* by
604 methionyl-tRNA. *Proc. Natl. Acad. Sci. U. S. A.* **73**, 1664–8 (1976).
- 605 35. Lee, S. S., Avalos Vizcarra, I., Huberts, D. H. E. W., Lee, L. P. & Heinemann, M. Whole lifespan
606 microscopic observation of budding yeast aging through a microfluidic dissection platform.
607 *Proc. Natl. Acad. Sci. U. S. A.* **109**, 4916–20 (2012).
- 608 36. Huberts, D. H. E. W. *et al.* Construction and use of a microfluidic dissection platform for long-
609 term imaging of cellular processes in budding yeast. *Nat. Protoc.* **8**, 1019–27 (2013).
- 610 37. Elbing, K. *et al.* Role of hexose transport in control of glycolytic flux in *Saccharomyces*
611 *cerevisiae*. *Appl. Environ. Microbiol.* **70**, 5323–30 (2004).
- 612 38. Yoshioka, K. *et al.* A novel fluorescent derivative of glucose applicable to the assessment of
613 glucose uptake activity of *Escherichia coli*. *Biochim. Biophys. Acta* **1289**, 5–9 (1996).
- 614 39. Snoep, J. L., Mrwebi, M., Schuurmans, J. M., Rohwer, J. M. & Teixeira de Mattos, M. J. Control
615 of specific growth rate in *Saccharomyces cerevisiae*. *Microbiology* **155**, 1699–1707 (2009).
- 616 40. Youk, H. & van Oudenaarden, A. Growth landscape formed by perception and import of
617 glucose in yeast. *Nature* **462**, 875–9 (2009).
- 618 41. Otterstedt, K. *et al.* Switching the mode of metabolism in the yeast *Saccharomyces cerevisiae*.
619 *EMBO Rep.* **5**, 532–7 (2004).
- 620 42. Novak, S., Zechner-Krpan, V. & Marić, V. Regulation of Maltose Transport and Metabolism in
621 *Saccharomyces cerevisiae*. *Food Technol Biotech* 213–218 (2004).
- 622 43. Blount, B. A., Weenink, T., Vasylechko, S. & Ellis, T. Rational diversification of a promoter
623 providing fine-tuned expression and orthogonal regulation for synthetic biology. *PLoS One* **7**,
624 e33279 (2012).
- 625 44. Gustavsson, A.-K. *et al.* Sustained glycolytic oscillations in individual isolated yeast cells. *FEBS*
626 *J.* **279**, 2837–47 (2012).
- 627 45. Aon, M. A. *et al.* Dynamic regulation of yeast glycolytic oscillations by mitochondrial functions.
628 *J. Cell Sci.* **99 (Pt 2)**, 325–34 (1991).
- 629 46. Kang, H. T. & Hwang, E. S. 2-Deoxyglucose: an anticancer and antiviral therapeutic, but not
630 any more a low glucose mimetic. *Life Sci.* **78**, 1392–9 (2006).
- 631 47. de Felipe, P. *et al.* E unum pluribus: multiple proteins from a self-processing polyprotein.
632 *Trends Biotechnol.* **24**, 68–75 (2006).

- 633 48. Edgington, N. P. & Futcher, B. Relationship between the function and the location of G1
634 cyclins in *S. cerevisiae*. *J. Cell Sci.* **114**, 4599–611 (2001).
- 635 49. Jorgensen, P. *et al.* The size of the nucleus increases as yeast cells grow. *Mol. Biol. Cell* **18**,
636 3523–32 (2007).
- 637 50. Webster, M., Witkin, K. L. & Cohen-Fix, O. Sizing up the nucleus: nuclear shape, size and
638 nuclear-envelope assembly. *J. Cell Sci.* **122**, 1477–86 (2009).
- 639 51. Nishimura, K., Fukagawa, T., Takisawa, H., Kakimoto, T. & Kanemaki, M. An auxin-based
640 degron system for the rapid depletion of proteins in nonplant cells. *Nat. Methods* **6**, 917–922
641 (2009).
- 642 52. Papagiannakis, A., de Jonge, J. J., Zhang, Z. & Heinemann, M. Quantitative characterization of
643 the auxin-inducible degron: a guide for dynamic protein depletion in single yeast cells. *Sci.*
644 *Rep.* **7**, 4704 (2017).
- 645 53. Leupold, S. *et al.* *Saccharomyces cerevisiae* goes through distinct metabolic phases during its
646 replicative lifespan. *Elife* **8**, (2019).
- 647 54. Lew, D. J. & Reed, S. I. Morphogenesis in the yeast cell cycle: regulation by Cdc28 and cyclins.
648 *J. Cell Biol.* **120**, 1305–20 (1993).
- 649 55. Bryan, A. K., Goranov, A., Amon, A. & Manalis, S. R. Measurement of mass, density, and
650 volume during the cell cycle of yeast. *Proc. Natl. Acad. Sci. U. S. A.* **107**, 999–1004 (2010).
- 651 56. Parisi, E., Yahya, G., Flores, A. & Aldea, M. Cdc48/p97 segregase is modulated by cyclin-
652 dependent kinase to determine cyclin fate during G1 progression. *EMBO J.* **37**, e98724 (2018).
- 653 57. Futcher, B. Metabolic cycle, cell cycle, and the finishing kick to Start. *Genome Biol.* **7**, 107
654 (2006).
- 655 58. Wullschleger, S., Loewith, R. & Hall, M. N. TOR signaling in growth and metabolism. *Cell* **124**,
656 471–84 (2006).
- 657 59. Lindqvist, L. M., Tandoc, K., Topisirovic, I. & Furic, L. Cross-talk between protein synthesis,
658 energy metabolism and autophagy in cancer. *Curr. Opin. Genet. Dev.* **48**, 104–111 (2018).
- 659 60. Moore, S. A. Kinetic evidence for a critical rate of protein synthesis in the *Saccharomyces*
660 *cerevisiae* yeast cell cycle. *J. Biol. Chem.* **263**, 9674–81 (1988).
- 661 61. Peregrín-Alvarez, J. M., Sanford, C. & Parkinson, J. The conservation and evolutionary
662 modularity of metabolism. *Genome Biol.* **10**, R63 (2009).
- 663 62. Bertoli, C., Skotheim, J. M. & de Bruin, R. A. M. Control of cell cycle transcription during G1
664 and S phases. *Nat. Rev. Mol. Cell Biol.* **14**, 518–28 (2013).
- 665
- 666

1 **Methods**

3 Yeast Strains

4 Prototrophic *Saccharomyces cerevisiae* strains of the CEN.PK and S288C backgrounds were used in this
5 study. All strains used are listed in Supplementary Table 1. Genomic integrations of fluorescent
6 reporters were carried out using standard PCR-based strategies to amplify resistance cassettes with
7 the respective fluorescent protein and appropriate, typically ~300-500 bp long, flanking sequences,
8 and C-terminal insertion to the target gene by homologous recombination⁶³. Unless indicated
9 otherwise, constructs for TEF1 and Tet-ON driven expression of GFP, as well as for Tet-ON driven
10 expression of Hxt1, were incorporated in the HO genomic locus. The full list of primers and information
11 on how they were used in strain construction are presented in Supplementary Table 2.

12 Yeast Growth Media and Procedures

13 Synthetic minimal media (yeast nitrogen base without amino acids (Formedium) and minimal
14 medium⁶⁴ supplemented with the indicated concentrations of glucose, maltose, galactose, or lactate
15 (Sigma-Aldrich) were used throughout. Batch cultivation took place at 30°C at a shaking speed of 300
16 rpm. Cells from log-phase batch cultures were used to load the microfluidics device, and thereafter,
17 cells were continuously supplemented with fresh medium of the indicated composition. For nutrient
18 shifts during microfluidics cultivation, media were pre-incubated at 30°C.

19 Unless otherwise indicated, for experiments with low (0.01gL⁻¹) glucose, cells from late log-phase from
20 high (20 gL⁻¹) glucose cultures were used to inoculate low glucose media at an OD of 0.05. After
21 overnight cultivation, cells were loaded to the microfluidics device and were continuously
22 supplemented with fresh low glucose media for 8.5 to 9 hours before the initiation of the experiment
23 to allow for adaptation to the low glucose conditions.

24 For identification of percentage of wild-type G1 arrested cells as a function of glucose concentration
25 in the microfluidics device, cells for low glucose concentrations (<10 gL⁻¹) were grown to log phase in
26 media with 10 gL⁻¹ glucose, were then transferred to media with the appropriate low concentration of
27 glucose for ~4 hours, and were subsequently loaded to the microfluidics device. Upon loading of the
28 microfluidics device, cells were continuously fed with media containing the appropriate concentration
29 of glucose, and were monitored for 12 hours to assess their capacity to progress from G1 to S phase,
30 by observing the appearance of the bud cell. Cells that were already undergoing cell division at the
31 time of loading, were allowed to complete their current cell division cycle before assessed for G1 arrest
32 for the next 12 hours.

33 For obtaining large daughter cells, wild type cells from log-phase cultures were loaded to the
34 microfluidics device and were allowed to replicatively age for ≈ 22 hours, before initiating fluorescent
35 measurements. The large daughters of these replicatively-aged mother cells were then used for further
36 analyses.

37 Microscopy and imaging

38 Widefield microscopy was performed using a microfluidics dissection platform³⁶ mounted to inverted
39 fluorescence microscopes (Eclipse Ti-E; Nikon instruments). The temperature was retained constant at
40 30°C using a microscope incubator (Life Imaging Services GmbH). Images were recorded using an iXon
41 Ultra 897 DU-897-U-CD0-#EX camera (Andor Technology Ltd). During brightfield imaging a UV blocking
42 filter was used. Fluorescent measurements were performed using an LED-based excitation system
43 (pE2; CoolLED Limited). Fluctuations in axial focus during time-lapse imaging were corrected using
44 automated hardware (PFS; Nikon). Fluorescent measurements for estimation of dynamic protein
45 production rates and Whi5 concentration were performed with 100x objectives. Widefield microscopy
46 settings are presented in Supplementary Table 3. Time-lapse confocal microscopy was performed with
47 a Zeiss LSM800 confocal microscope and photomultiplier tubes by Hamamatsu Photonics, using agar
48 slabs perfused in 20 gL⁻¹ glucose medium. A 63x oil immersion objective was used. Temperature was
49 kept at 30°C throughout the experiments using an incubator chamber and a controlled heated
50 objective ring. GFP fluorescence for TEF1-sfGFP and Whi5-sfGFP was analysed by excitation with a 488
51 nm laser (2% light intensity; 0.56 μ s dwell-time exposure) and emission was detected using a 490-535
52 nm band-pass filter. For every imaging position five z-axis planes with a 0.6 μ m step were acquired
53 every 5 min.

54 To avoid photobleaching related artefacts, especially with respect to Whi5 measurements, more
55 photostable fluorescent proteins^{65,66} in comparison to what was used earlier¹³ were used, and the
56 imaging frequency was adjusted according to the growth conditions, and thus, to the total amount of
57 light received by the fluorescent proteins during G1. On the other hand, in confocal microscopy (where
58 the light intensities used are considerably higher and some degree of photobleaching is inevitable), we
59 corrected our images for photobleaching, as detailed in the *Image Analysis* section.

60 Image analysis

61 *Cell segmentation and fluorescence measurements*

62 Cell segmentation for cell volume and fluorescence intensity measurements were performed using the
63 semi-automated ImageJ plugin BudJ²³ (<http://www.ibmb.csic.es/home/maldea>). The compartment of
64 the mother and bud cells were segmented independently and the respective cell volumes were
65 thereafter combined²³. For validation, cell volume and fluorescent measurements were performed for

66 specific cells also manually using ImageJ⁶⁷, assuming that the body of the cell approximates a prolate
67 ellipsoid. Fluorescent intensity measurements were corrected for background autofluorescence
68 before any further analysis, by subtracting the modal fluorescence value of the whole image from the
69 mean cellular fluorescence at each time point. Cell-cycle and cell-size related changes in
70 autofluorescence did not have any significant influence on the measured fluorescence dynamics
71 (Extended Data Figures 2e, 4g and 5a). Unless specified otherwise, total cellular fluorescence was
72 estimated by multiplying the cell volume with the mean cellular fluorescence at each time point.
73 Verification analyses for widefield measurements were performed also by estimating total cellular
74 fluorescence via integrating fluorescence over the whole cell area. In one case where we observed
75 uneven illumination across the y-axis of the field of view, we corrected for this effect by first
76 determining the fluorescence intensity of cells as a function of the y-coordinate of the field of view.
77 Then, since a linear dependency on the y-coordinate of the field of view and the fluorescence intensity
78 was observed, we generated a linear function to describe this dependency, with which we corrected
79 the original image to obtain the flat-field image⁶⁸. Cytokinesis was determined by the darkening of the
80 bud neck on brightfield images⁶⁹. Start was defined as the first time point after the exit of Whi5-GFP
81 or Whi5-mCherry from the nucleus, determined by visual inspection of microscopy images⁷⁰. G1 was
82 defined as the period between cytokinesis and bud appearance. Confocal images analysis was
83 conducted also using ImageJ, BudJ, and a custom-made Python script (available from GitHub at
84 <https://github.com/molecular-systems-biology/Litsios-et-al-2019>; DOI: 10.5281/zenodo.3455842).
85 Mean cell fluorescence was calculated in all z-axis stacks using the cell boundary detected by BudJ, and
86 pixels with intensity value below the 50-percentile of the whole cell were excluded to avoid erroneous
87 signals from vacuoles. The value of the stack with the maximum mean fluorescence intensity was
88 chosen for further estimations. To correct for photobleaching, the mean GFP fluorescent intensities of
89 every cell at every time point were averaged and a decreasing exponential function was fitted. The
90 function was normalized for its first value ($t = 0$) and the inverse of the normalized photobleaching
91 function value at each time point was used to correct the original signal from each cell.

92 *Processing of single-cell time series data*

93 The time series describing the time evolution of different single-cell quantities were processed with a
94 computational pipeline based on Gaussian processes (GPs), a class of powerful and flexible non-
95 parametric Bayesian models that are used to define distributions over functions⁷¹. GP-based regression
96 on noisy data combines in a natural way our prior beliefs about features of the underlying function
97 (e.g. smoothness, relevant time scales etc.) with the measurement uncertainty into a posterior
98 probability distribution which reflects the residual uncertainty about the function that gave rise to the
99 observed data. The GP posterior can be used to predict the underlying function values and their

100 associated uncertainty at any time point. Moreover, since the derivative of a GP is another GP⁷², the
101 time-derivative of the measured time-series and be analytically estimated from the GP posterior
102 obtained from the measurements. Further information and background on Gaussian processes can be
103 found in^{71,73}.

104 Concretely, our data-processing pipeline for each single-cell quantity (total fluorescence, cell volume,
105 NAD(P)H fluorescence time series) comprised the following steps: (i) Manual inspection of each single-
106 cell trajectory for obvious artefacts, such as those generated by failed mother/bud cell tracking and
107 shifts in focus, which result in large, sudden jumps in measured cell volumes and/or fluorescence. To
108 avoid biasing the results, single-cell trajectories affected by such artefacts were discarded. (ii) GP-
109 based smoothing of each single-cell time series using a GP prior with zero mean and a rational
110 quadratic covariance function⁷¹. The hyperparameters of the covariance function were estimated by
111 maximizing the marginal likelihood of the measured data using multistart optimization started from
112 20 random initial points and retaining the best of these runs. At the end of this step, an optimized
113 posterior GP was obtained for every single-cell trajectory. (iii) Calculation of the posterior predictive
114 mean and variance over a dense grid of time points. (iv) Estimation of the mean and variance of the
115 derivative process based on the data of Step (iii). GP fitting (hyperparameter optimization) and
116 posterior-based predictions were carried out using the GPML Matlab toolbox⁷⁴. To estimate
117 derivatives, we used a custom-made Matlab script based on the mathematical results presented in⁷².

118 In order to simplify the analysis and avoid the unnecessary amplification of measurement noise by
119 additional data-processing steps, the maturation half-life of sfGFP was assumed to be negligible during
120 the processing of fluorescence measurements. This choice was justified based on estimates of the
121 sfGFP maturation rate, which corresponds to a half-time of about 5 min⁷⁵. Moreover, as demonstrated
122 in⁷⁶, taking into account such a short maturation half-life has negligible impact on the estimated
123 protein production kinetics.

124 2-NBDG based glucose uptake rate assay

125 For comparing the glucose uptake rate in coexisting G1-arrested and dividing cells of the TM6* strain,
126 cells were cultivated in the microfluidics device in 10 gL⁻¹ glucose and subsequently switched to 0.01
127 gL⁻¹ glucose plus 60 μM 2-NBDG for 25 min. The ratio of cellular fluorescence at 470 nm
128 (Supplementary Table 3) right after and before the treatment with 2-NBDG was estimated for both
129 dividing and G1-arrested cells. Cells were identified as G1-arrested if they did not bud for at least 24
130 hours.

131 Characterization of TM6* physiology during growth on glucose and maltose

132 For characterization of TM6* physiology on glucose and maltose, log-phase cultures with the
 133 respective carbon source at 10 gL⁻¹ concentration were sampled every 60 or 120 min to determine
 134 growth by OD_{600nm} measurements and cell count by flow cytometry (BD Accuri C6; BD Biosciences).
 135 Levels of glucose or maltose and extracellular metabolites were determined every 60 or 120 min by
 136 collecting 0.2 mL of culture and centrifuging for 5 min at 13200 rpm. The cell-free supernatant was
 137 transferred to filter columns of 0.22 pore size (SpinX; Corning Inc), spun for 15 s, and the flow-through
 138 was transferred to an HPLC vial for HPLC analysis (Agilent 1290 LC System; Agilent Technologies) using
 139 a Hi-Plex H column with 5 mM H₂SO₄ as eluent at a constant flow rate of 0.6 mL min⁻¹ and column
 140 temperature of 60°C. Chromatogram integration was done with Agilent Open Lab CDS software. As a
 141 reference, the physiology of KOY.PK2-1C83 (wild type) strain was measured in the same way on 10 gL⁻¹
 142 ¹ glucose. Data were obtained from at least 3 biological replicates for each stain at each tested
 143 condition. Dry cell weight was determined by culture filtering through pre-weighed nitrocellulose 0.2
 144 2 µm pore size filters (Whatman; GE Healthcare Life Sciences), and re-weighting after dry-incubation
 145 at 80°C. The cell count of the culture right before filtration was used to calculate the dry weight per
 146 cell of the examined strain at the respective nutrient condition. Oxygen and carbon dioxide transfer
 147 rates were determined every 30 min using the online gas exhaust monitoring system RAMOS (Kühner
 148 AG)⁷⁷. For RAMOS measurements, media were inoculated from the same cultures used to inoculate
 149 the cultures for the determination of glucose, maltose and ethanol concentrations, and cultivations
 150 were run in parallel.

151 Regression analysis was performed in gPROMS using an exponential growth model consisting of the
 152 following equations:

$$153 \quad \frac{d}{dt}X = \mu * X$$

$$154 \quad \frac{dc_S}{dt} = -X * q_S$$

$$155 \quad q_S = \frac{\mu}{Y_{xS}}$$

156
 157
 158
 159 For each extracellular metabolite the following equations were used:

$$160 \quad \frac{dc_P}{dt} = X * q_P$$

$$161 \quad q_P = \frac{Y_{pS}}{Y_{xS}}$$

162
 163 Where:

164 X : [g_{dcw}/l] biomass concentration

165 c_s : [g/l] substrate concentration
166 c_p : [g/l] product concentration
167 μ : [h^{-1}] biomass growth rate
168 q_s : [g/(g_{dcw} * h)] specific glucose uptake rate
169 q_p : [g/(g_{dcw} * h)] specific production rate
170 Y_{xs} : [g_{dcw}/g] biomass yield
171 Y_{ps} : [g/g] product yield

172 Characterization of the Tet-On Hxt1 system

173 To characterize the tetracycline-inducible HXT1 expression system a log-phase culture (10 gL⁻¹ maltose)
174 was centrifuged (4 min; 300 rpm), medium was removed, and cells were resuspended in 1 mL fresh
175 glucose (10 gL⁻¹) medium, which was used to inoculate new glucose (10 gL⁻¹) cultures containing a range
176 of tetracycline concentrations. Hxt1-GFP fluorescence was followed by flow cytometry every 60 min.
177 Measurements during 3-8 h period after inoculation, during which steady HXT1-GFP expression was
178 achieved, were used to estimate the mean Hxt1-GFP fluorescence per condition. As a control for leaky
179 Hxt1-GFP expression, cultures without tetracycline were followed. As a control for cellular
180 autofluorescence, a culture of *VW100 tet-Hxt1* without tetracycline was followed. To correct for
181 fluorescence of the tetracycline molecules at the GFP spectrum, *VW100 tet-Hxt1* cells were incubated
182 for ≈1 hour in glucose (10 gL⁻¹) medium containing all the range of the tested tetracycline
183 concentrations. An effect of tetracycline on cellular autofluorescence was observed at tetracycline
184 concentrations of 200 ng mL⁻¹ and higher, and the level of tetracycline-related autofluorescence was
185 subtracted from the *VW100 tet-Hxt1-GFP* measurements at the respective concentrations.

186 Comparison of single-cell Cln3 measurements with population-based Cln3 data from Blank *et al.*²⁷

187 For Extended Data Figure 4d, the mean concentration of Cln3 during G1 for each cell was measured in
188 cells growing on 20 gL⁻¹ glucose (n=41), 20 gL⁻¹ galactose (n=36), and 20 gL⁻¹ lactate (n=43), and
189 doubling time was estimated by determining the time between cell birth and completion of the first
190 division cycle (cytokinesis) for single cells growing at the respective nutrient conditions (n=36, 29, and
191 14 respectively). To compare our single-cell Cln3 measurements across different growth conditions
192 with respective population-based measurements of a recent study²⁷, Cln3 data from Figure 4A from
193 Blank et al (2018) were digitized using PlotDigitizer 2.6.8. For direct comparison with our single-cell
194 data, the mean was calculated for Cln3 levels and doubling times corresponding to measurements
195 from similar doubling times in the study of Blank et al (2018). Specifically, data from the following
196 ranges of doubling times were grouped together: 2.43-2.78 hours, n=7; 3.05-3.09 hours, n=3; 7.99-
197 8.14 hours, n=3.

198 Measurement of Cln3 and Whi5 via targeted proteomics in cell-cycle-synchronous cultures

199 *Elutriation and sampling*

200 For the targeted proteomics experiments, single wild type colonies were used to inoculate liquid YPD
201 cultures. After overnight growth, cultures were diluted in fresh media at an $OD_{600} = 0.5-1$ and were
202 allowed to undergo $\approx 2-3$ cell divisions before harvested for elutriation. Elutriation was performed
203 similarly as described previously⁷⁸. 100 mL cultures were loaded into a large elutriation chamber (40
204 mL) at a pump speed of $40 \text{ mL} \cdot \text{min}^{-1}$ and rotor speed of 3200 rpm. The elutriation buffer was YPD pre-
205 warmed at 30°C . Approximately 300 mL of media containing small-sized cells were collected by
206 increasing the pump speed to $65 \text{ mL} \cdot \text{min}^{-1}$. The elutriated cells were centrifuged at 3900 rpm for 2
207 min, re-suspended in 35 mL of pre-warmed YPD and incubated at 30°C with shaking. Sampling took
208 place every 10 minutes. Specifically, 2 ml of culture was centrifuged (30 sec; 11000 rcf), the
209 supernatant was discarded, and cells were flash-frozen in liquid nitrogen. At each time point, 100 μL
210 of culture was also used to measure the cell size distribution of the population using CASY® TT, and
211 200 μL of culture was fixed with 70% EtOH for determining the budding index via microscopy.

212 *Sample preparation*

213 Cell pellets were reconstituted in 40 μL 2% sodium-deoxycholate; 7.5 mM TECEP; 100mM
214 ammoniumbicarbonate and sonicated twice for 10 seconds using a UP200St with VialTweeter
215 (HielscherUltrasonics GmbH). Heat treatment was performed for 10 minutes at 95°C . After cooling,
216 concentration was determined by BCA assay (Thermo, 23252) and 100 μg protein per sample was used
217 for subsequent steps. Alkylation was performed by addition of iodoacetamide to a final concentration
218 of 40 mM and incubation for 45 minutes in the dark at RT. Samples were diluted 1:2 using 100 mM
219 ammoniumbicarbonate, and mass spectrometry grade Trypsin (Promega, V5280) was added at a ratio
220 of 1:50 (μg Trypsin: μg Protein) and incubated overnight at 37°C at 400 rpm. The reaction was stopped
221 by adding trifluoroacetic acid to a final concentration of 1%. Sample cleanup by solid phase extraction
222 was performed with Pierce® C18 tips (Thermo, 87784) according to the supplier's manual. The eluate
223 fraction was dried under vacuum and reconstituted with 20 μL 2% acetonitrile, 0.1% formic acid.

224 *Targeted PRM-LC-MS analysis of selected peptides/proteins*

225 In a first step, parallel reaction-monitoring (PRM) assays⁷⁹ were generated from a mixture containing
226 500 fmol of each heavy reference peptide (JPT Peptide Technologies GmbH), iRT KIT peptides according
227 to the manufacturer's protocol (Biognosys, Schlieren, Switzerland), and shotgun data-dependent
228 acquisition (DDA) LC-MS/MS analysis on a Q-Exactive HF platform. The setup of the $\mu\text{RPLC-MS}$ system
229 was as described previously⁸⁰. Chromatographic separation of peptides was carried out using an EASY

230 nano-LC 1000 system (Thermo Fisher Scientific), equipped with a heated RP-HPLC column (75 μm x 30
231 cm) packed in-house with 1.9 μm C18 resin (Reposil-AQ Pur, Dr. Maisch). Peptides were analysed per
232 LC-MS/MS run using a linear gradient ranging from 95% solvent A (0.1% formic acid in water (v/v)) and
233 5% solvent B (80% acetonitrile, 19.9% water, 0.1% formic acid (v/v/v)) to 45% solvent B over 60 minutes
234 at a flow rate of 200 $\text{nL}\cdot\text{min}^{-1}$. Mass spectrometry analysis was performed on Q-Exactive HF mass
235 spectrometer equipped with a nanoelectrospray ion source (both Thermo Fisher Scientific). Each MS1
236 scan was followed by high-collision-dissociation (HCD) of the 10 most abundant precursor ions with
237 dynamic exclusion for 20 seconds. Total cycle time was approximately 1 s. For MS1, 3e^6 ions were
238 accumulated in the Orbitrap cell over a maximum time of 100 ms and scanned at a resolution of
239 120,000 FWHM (at 200 $\text{m}\cdot\text{z}^{-1}$). MS2 scans were acquired at a target setting of 1e^5 ions, accumulation
240 time of 50 ms and a resolution of 30,000 FWHM (at 200 $\text{m}\cdot\text{z}^{-1}$). Singly charged ions and ions with
241 unassigned charge state were excluded from triggering MS2 events. The normalized collision energy
242 was set to 28%, the mass isolation window was set to 1.4 $\text{m}\cdot\text{z}^{-1}$ and one microscan was acquired for
243 each spectrum.

244 The acquired raw-files were searched against a yeast database (UniProt: download date: 30/10/2014,
245 total of 6,652 entries) by the MaxQuant software (Version 1.0.13.13) using default parameters. The
246 best 6 transitions for each peptide were selected automatically using an in-house software tool and
247 imported to Spectrodive software (version 7.5). A mass isolation lists containing 2 peptides for each
248 protein was exported from Spectrodive and imported into the Orbitrap Fusion Lumos operating
249 software for PRM analysis. The complete list of peptides and transitions used for PRM analysis are
250 shown in Supplementary Table 4. Chromatographic separation of peptides was carried out using an
251 EASY nano-LC 1200 system (Thermo Fisher Scientific), equipped with a heated RP-HPLC column (75 μm
252 x 37 cm) packed in-house with 1.9 μm C18 resin (Reposil-AQ Pur, Dr. Maisch). For PRM analysis,
253 peptide samples were prepared as described above and spiked with the heavy reference peptide mix
254 above at 2 fmol/peptide/ μg of total peptide mass. The peptides were separated using a following
255 stepwise gradient: from 95% solvent A (0.1% formic acid in water (v/v)) and 5% solvent B (80%
256 acetonitrile, 19.9% water, 0.1% formic acid (v/v/v)) to 28% solvent B until 45 minutes and then to 45%
257 solvent B until 60 minutes at the constant flow rate of 200 $\text{nL}\cdot\text{min}^{-1}$. For the PRM-MS analysis (MS2
258 scans), the resolution of the orbitrap was set to 120,000 FWHM (at 200 $\text{m}\cdot\text{z}^{-1}$) and the fill time was set
259 to 250 ms to reach a target value of 1e^6 ions. Ion isolation window was set to 0.4 Th. For each MS cycle,
260 a full MS1 scan at 60,000 FWHM (at 200 $\text{m}\cdot\text{z}^{-1}$) was included. In addition, a few selected samples were
261 also analyzed in DDA mode using the same LC gradient and parameters as above. After database
262 searching (using MaxQuant and parameters as above) proteotypic peptides for three abundant yeast
263 proteins (Glyceraldehyde-3-phosphate dehydrogenase 3, Enolase 2 and Actin, two peptides for each

264 protein) were extracted and used for normalizing the PRM results for starting material variations
265 (details see below).

266 *Quantitative analysis*

267 The PRM files were imported and processed using the Spectrodrive software with the default settings.
268 For each target peptide, the total peak areas of the most intense transitions were exported. Only
269 peptides with the Elution Group Q.Value <0.01 were considered for quantitative analysis.
270 Subsequently, the raw files were imported into the Skyline software (version 4.2) to extract and sum
271 the MS1 intensities of peptide ions belonging to constitutively expressed proteins (Glyceraldehyde-3-
272 phosphate dehydrogenase 3, Enolase 2 and Actin, two peptides for each protein were selected). PRM
273 (MS2) intensities of target peptides were then normalized to the summed (MS1) intensity of selected
274 peptides from the constitutively expressed proteins. The obtained normalized intensities were divided
275 by the median of all samples to shift the final expression values into a meaningful scale of around 1.
276 The mean of the different peptides from each protein was then estimated for each time point for each
277 replicate experiment.

278 Dynamic depletion of Cln3 in single cells

279 The uncoupling of Cln3 levels from the overall protein production dynamics was performed as
280 described in Figure 5e, by tagging the endogenous Cln3 with an auxin-inducible degron (AID)^{48,49}, and
281 using either 1 or 2 mM of the synthetic auxin substitute naphthalene-acetic acid (NAA) to activate
282 depletion. To allow for sufficient activation of depletion, G1 duration was estimated for both Cln3-AID
283 and control, in cells that entered G1 either 15 or 30 min after addition of NAA (1 or 2 mM respectively).

284 The effect of protein degradation on protein abundance dynamics

285 Consider a simple model of protein synthesis and degradation. In this model, the abundance of a
286 protein P (denoted by p) follows the rate equation

$$287 \quad \frac{dp}{dt} = k_p(t) - k_d p, \quad (1)$$

288 where $k_p(t)$ is the (possibly time-varying) synthesis rate and k_d the degradation rate. We consider
289 two limiting situations: one in which k_d is very large, leading to a very short protein half-life, and one
290 in which $k_d = 0$, corresponding to a highly stable protein such as GFP.

291 To understand the dynamics of $p(t)$ for large k_d , we can turn to the analysis of the linear system (1)
292 in the frequency domain⁸¹. Viewing the synthesis rate $k_p(t)$ as the system input and $p(t)$ as the output,
293 frequency-response theory tells us that the output will closely track input signals with frequency
294 content smaller than the *bandwidth* of the system, which ranges from the zero frequency up to $f_{BW} =$
295 $k_d/2\pi$ (corresponding to a period of k_d^{-1}). As k_d increases, the range of frequencies over which the

296 output will be proportional to the input will increase as well. To get a sense of the relevant time scales,
297 for a protein with half-life of 5 minutes ($k_d = \log(2)/5 = 0.139 \text{ min}^{-1}$) the protein abundance will
298 very closely track inputs that vary over time scales *longer* than $k_d^{-1} = 7.2 \text{ min}$.

299 Put in more intuitive terms, when k_d is very large, the protein abundance tends to equilibrate very fast
300 in response to changes in the synthesis rate. For a fixed synthesis rate, $k_{p,0}$, the equilibrium protein
301 abundance is equal to $k_{p,0}/k_d$. Consequently, for a time-varying synthesis rate and large k_d , protein
302 abundance will be very close to $k_p(t)/k_d$. This result is also known as the *quasi steady-state*
303 *approximation*⁸¹ in the theory of chemical kinetics. Finally, it should be noted that keeping $k_p(t)$ the
304 same, increasing k_d will also decrease the average levels of the protein.

305 When $k_d = 0$, equation (1) shows that $p(t)$ will be given by

306
$$p(t) = p(0) + \int_0^t k_p(s) ds,$$

307 where $p(0)$ is the amount of protein present at time zero. The stark contrast between the responses
308 of eq. (1) in the two limiting cases (large vs. zero k_d) is displayed in Extended Data Figure 8.

309

310 Statistics and Reproducibility

311 Statistical analyses were performed using Matlab and GraphPad Prism. Whenever applicable, two-
312 sided statistical tests were performed. Experiments related to Figure 1d and Extended Data Figure 4b
313 were performed once with multiple imaging positions. Overall, sample sizes, measures of centrality
314 and dispersion, statistical tests and p-values, are reported when applicable in the figures and their
315 respective captions. For non-graphically reported data, this information is included in the main text.

316

317 **Data Availability**

318 Source data for Figures 1-6 and Extended Data Figures 1-8 are provided in Source Data. The mass
319 spectrometry proteomics data have been deposited to the ProteomeXchange Consortium via the
320 PRIDE⁸² partner repository with the dataset identifier PXD015327. All other data are available from the
321 authors on reasonable request.

322

323 **Code Availability**

324 At <https://github.com/molecular-systems-biology/Litsios-et-al-2019> (DOI: 10.5281/zenodo.3455842),
325 we provide one CSV file with raw microscopy data together with the respective Matlab file in which
326 the data processing (smoothing, rate estimation etc.) is performed, as an example of our data
327 processing pipeline. These data were used in the construction of Fig. 5c of the main text and

328 Extended Data Figure 4h. The custom-made Python script used for analysis of confocal images is also
329 provided. All other Matlab scripts used for processing are available from the authors on reasonable
330 request.

331

332 REFERENCES

- 333 63. Wach, A. PCR-synthesis of marker cassettes with long flanking homology regions for gene
334 disruptions in *S. cerevisiae*. *Yeast* **12**, 259–65 (1996).
- 335 64. Verduyn, C., Postma, E., Scheffers, W. A. & Van Dijken, J. P. Effect of benzoic acid on metabolic
336 fluxes in yeasts: a continuous-culture study on the regulation of respiration and alcoholic
337 fermentation. *Yeast* **8**, 501–17 (1992).
- 338 65. Shaner, N. C., Steinbach, P. A. & Tsien, R. Y. A guide to choosing fluorescent proteins. *Nat.*
339 *Methods* **2**, 905–909 (2005).
- 340 66. Shaner, N. C. *et al.* A bright monomeric green fluorescent protein derived from
341 *Branchiostoma lanceolatum*. *Nat. Methods* **10**, 407–9 (2013).
- 342 67. Schindelin, J. *et al.* Fiji: an open-source platform for biological-image analysis. *Nat. Methods* **9**,
343 676–82 (2012).
- 344 68. Waters, J. C. Accuracy and precision in quantitative fluorescence microscopy. *J. Cell Biol.* **185**,
345 1135–48 (2009).
- 346 69. Zopf, C. J., Quinn, K., Zeidman, J. & Maheshri, N. Cell-cycle dependence of transcription
347 dominates noise in gene expression. *PLoS Comput. Biol.* **9**, e1003161 (2013).
- 348 70. Doncic, A., Falleur-Fettig, M. & Skotheim, J. M. Distinct interactions select and maintain a
349 specific cell fate. *Mol. Cell* **43**, 528–39 (2011).
- 350 71. Rasmussen, C. E. & Williams, C. K. I. *Gaussian processes for machine learning*. (MIT Press,
351 2006).
- 352 72. Swain, P. S. *et al.* Inferring time derivatives including cell growth rates using Gaussian
353 processes. *Nat. Commun.* **7**, 13766 (2016).
- 354 73. MacKay, D. J. C. *Information theory, inference, and learning algorithms*. (Cambridge University
355 Press, 2003).
- 356 74. Rasmussen, C. E. & Nickisch, H. Gaussian Processes for Machine Learning (GPML) Toolbox. *J.*
357 *Mach. Learn. Res.* **11**, 3011–3015 (2010).
- 358 75. Khmelinskii, A. *et al.* Tandem fluorescent protein timers for in vivo analysis of protein
359 dynamics. *Nat. Biotechnol.* **30**, 708–14 (2012).
- 360 76. Wang, X., Errede, B. & Elston, T. C. Mathematical analysis and quantification of fluorescent
361 proteins as transcriptional reporters. *Biophys. J.* **94**, 2017–26 (2008).
- 362 77. Anderlei, T., Zang, W., Papaspyrou, M. & Büchs, J. Online respiration activity measurement
363 (OTR, CTR, RQ) in shake flasks. *Biochem. Eng. J.* **17**, 187–194 (2004).
- 364 78. Rosebrock, A. P. Synchronization of Budding Yeast by Centrifugal Elutriation. *Cold Spring Harb.*

- 365 *Protoc.* **2017**, pdb.prot088732 (2017).
- 366 79. Peterson, A. C., Russell, J. D., Bailey, D. J., Westphall, M. S. & Coon, J. J. Parallel reaction
367 monitoring for high resolution and high mass accuracy quantitative, targeted proteomics.
368 *Mol. Cell. Proteomics* **11**, 1475–88 (2012).
- 369 80. Ahrné, E. *et al.* Evaluation and Improvement of Quantification Accuracy in Isobaric Mass Tag-
370 Based Protein Quantification Experiments. *J. Proteome Res.* **15**, 2537–47 (2016).
- 371 81. Del Vecchio, D. & Murray, R. M. *Biomolecular feedback systems*. (Princeton University Press
372 Princeton, NJ, 2015).
- 373 82. Perez-Riverol, Y. *et al.* The PRIDE database and related tools and resources in 2019: Improving
374 support for quantification data. *Nucleic Acids Res.* **47**, D442–D450 (2019).
- 375